A Genetically Encoded and Versatile Probe for Fluorescence Polarization Detection

Authors: Ayana Sugizaki[1,2,7], Keisuke Sato[1,2,7], Kazuyoshi Chiba[3], Kenta Saito[1,2], Masahiko Kawagishi[1,2], Yuri Tomabechi[4], Shalin B. Mehta[5,8], Hirokazu Ishii[5,9], Naoki Sakai[4,10], Mikako Shirouzu[4], Tomomi Tani[5,6], Sumio Terada[1,2]*

Affiliations:

[1]Department of Neuroanatomy and Cellular Neurobiology, Graduate School of Medical and Dental Sciences, Tokyo Medical and Dental University, 1-5-45 Yushima, Bunkyo-ku, Tokyo 113-8519, Japan

[2]Center for Brain Integration Research, Tokyo Medical and Dental University, 1-5-45 Yushima, Bunkyo-ku, Tokyo 113-8519, Japan

[3]Department of Biological Sciences, Ochanomizu University, 2-1-1 Ohtsuka, Bunkyo-ku, Tokyo 112-8610, Japan

[4]RIKEN Center for Biosystems Dynamics Research, Suehiro-cho, Tsurumi-ku, Yokohama 230-0045, Japan.

[5]Eugene Bell Center for Regenerative Biology and Tissue Engineering, Marine Biological Laboratory, Woods Hole, MA 02543, USA

[6]Biomedical Research Institute, National Institute of Industrial Science and Technology, Ikeda, Osaka 563-8577, Japan

[7]These authors contributed equally to this work.

[8]Present Address: Advanced Optical Microscopy, Chan Zuckerberg Biohub, 499 Illinois Street, San Francisco, CA 94158, USA

[9]Present Address: Exploratory Research Center on Life and Living Systems (ExCELLS) and National Institute for Physiological Sciences (NIPS), National Institutes of Natural Sciences, 5-1 Higashiyama, Myodaiji-cho, Okazaki, Aichi 444-8787, Japan.

[10]Present Address: RIKEN SPring-8 Center, 1-1-1 Kouto, Sayo-cho, Sayo-gun, Hyogo 679-5148, Japan

*Correspondence author: terada.nana@tmd.ac.jp

Abstract: Monitoring molecular orientation is the key approach to study the spatial organization of molecular alignments within supramolecular complexes in living cells, but the opportunity is missing even with the latest super-resolution approaches. Fluorescence polarization microscopy (FPM) is a promising solution, but it is challenging to label target proteins with fluorescent probes in a sterically constrained manner, which is prerequisite for imaging with FPM. Here we report POLArIS, a genetically encoded and versatile probe for FPM. POLArIS is a recombinant binder with a rotationally constrained fluorescent protein and can target arbitrary biomolecules by combining with phage-display screening. Application of POLArIS that specifically binds to F-actin to live-imaging of starfish embryos revealed radially extended actin filaments in mitosis that had been escaping from previous observations. By taking advantage of the genetically encoded nature, POLArIS has a potential of supporting broader applications of fluorescence polarization techniques to a variety of living specimens.

Introduction

Fluorescence microscopy has been widely used to study the structures and the dynamics of sub-cellular biomolecular assemblies in living cells. Monitoring molecular orientation is the key approach to study the spatial organization of molecular alignments within supramolecular complexes. But considering the orientational dynamics of fluorescently labeled molecules is challenging even with the recent advancement of fluorescent microscopy including super-resolution approaches. Fluorophores, such as fluorescent proteins and organic compound dyes, emit fluorescence by radiating light as dipoles. The light emitted from a single dipole is fully polarized along the dipole axis. Therefore, when fluorescent labels are rigidly bound to molecules, the orientation of molecules can be monitored by analyzing the polarization state of the fluorescence. Fluorescence polarization microscopy (FPM) has been used for this approach (Kampmann et al., 2011; Mehta et al., 2016; Nakai et al., 2019; Nishizaka et al., 2004; Sosa et al., 2001; Swaminathan et al., 2017) and is especially useful for shedding light on the presence of orderly assembled molecules (DeMay et al., 2011; Vrabioiu and Mitchison, 2006, 2007). In addition, FPM can report molecular orientations at a single-molecule level even in living cells when target molecules are labeled at proper density (Mehta et al., 2016; Sosa et al., 2001).

Despite such promising advantages, FPM has not been widely used in biomedical research because of the difficulties in the labeling of target molecules with fluorescent proteins. To monitor the molecular orientation, a target molecule and a fluorescent protein must be rigidly connected so that the orientation of the target and that of the dipole of the fluorophore are sterically fixed, which is called constrained tagging. For many cases, intensive screening of the linkage is required, since the rational design of the constrained tagging is challenging. A novel, more versatile and easier approach is therefore imperative for expanding the application of FPM.

Recently, we reported that calponin homology domain of F-actin binding protein Utrophin (UtrCH) tagged with mEGFP in a constrained manner allowed us to observe the orientation of actin filaments with FPM (Nakai et al., 2019). Based on this successful "indirect" constrained tagging using a scaffold that specifically binds to target molecules, we have developed a more versatile fluorescent probe for FPM, named the Probe for Orientation and Localization of Arbitrary Intracellular Structures (POLArIS). POLArIS utilizes a recombinant binder that can be screened by phage-display to target arbitrary biomolecules of interests. As a proof of principle, we developed a POLArIS that specifically binds to F-actin ($POLArIS^{act}$) and demonstrated that $POLArIS^{act}$ reports the orientations of actin assembly with very high detection sensitivity. Moreover, by observing starfish embryos expressing $POLArIS^{act}$, we found a novel F-actin-based sub-cellular architecture that associates with the microtubule aster during mitosis, which had not been previously reported.

Results

Constrained tagging of a recombinant binder, Adhiron, with circularly permutated superfolder GFP

To develop POLArIS, we sought a recombinant binder protein that has a helix available for tagging with GFP, as most of successful constrained tagging approaches used direct connection of the C-terminal α-helices of target molecules to the N-terminal 3_{10} helix of GFP (Kampmann et al., 2011; Nakai et al., 2019; Vrabioiu and Mitchison, 2006, 2007). We found that Adhiron (the nomenclature was later changed to "affimer" (Bedford et al., 2017)), a small protein (~12 kDa) with a consensus sequence of plant-derived phytocystatins (Tiede et al., 2014), has an α-helix at its N-terminus lying on top of four anti-parallel β sheets (Figure 1A). Two variable peptide

regions are inserted between anti-parallel β sheets (Figure 1A) to create binding sites for an arbitrary molecule of interest, and phage-display screening is generally used for selecting Adhirons that specifically bind to target molecules (Hughes et al., 2017; Lopata et al., 2018). We chose specific three Adhirons (Adhiron-6, 14, and 24; for simplicity, we call them Ad-A, B, and C, respectively) that were reported to bind to F-actin *in vitro* (Lopata et al., 2016) as our initial test case. Affimers targeting F-actin were reported recently (Lopata et al., 2018), but we are not sure if these affimers are identical to the Adhirons used in this study due to the absence of sequence information in the report. The dissociation constant (K_d) of these Adhirons for F-actin was less than 0.5 μM, indicating that they bind to F-actin with a higher affinity than both Lifeact (K_d = 2.2 μM) (Riedl et al., 2008) and UtrCH (K_d = 19 μM) (Winder et al., 1995). To connect the N-terminal α-helix of Adhiron to the 3_{10} helix of GFP, we used a circularly-permutated superfolder GFP (sfGFP) recently developed in our lab (Figure 1A), which has the 3_{10} helix at its C-terminus and emits fluorescence comparably strong to the original sfGFP (Nakai et al., 2019) (hereinafter simply called cpGFP). The N-terminal region of Adhiron that does not form α-helix was deleted, and exposed terminal helices of Adhirons and cpGFP were connected with the peptide linker (L5) that was reported to form an α-helix (Arai et al., 2001). We made variations of Adhiron-cpGFP fusion constructs with extended α-helix linkers (L1-4), truncated α-helix linkers (L6-9), and constructs without any linkers (L10 and 11). No serious steric hindrance between cpGFP and Adhiron connected by candidate linkers was presumed by UCSF Chimera (Pettersen et al., 2004) inspection for all fusion proteins (Figure 1B shows an example for cpGFP-Ad-A L5). We also made a control construct (flex control) for each Adhiron by connecting cpGFP and Adhiron with a flexible linker.

Screening and characterization of POLArIS candidates for F-actin

First, we tested if flex controls are localized with F-actin in mammalian cells, as they are supposed to have the least steric hindrance. As shown in Figure S1A, exogenously expressed flex controls for cpGFP-Ad-A and C were co-localized with F-actin labeled with phalloidin-Atto565 in fixed HeLa cells. In contrast, cpGFP-Ad-B flex showed significant background fluorescence in cytoplasm and nucleus (arrows in Figure S1A), thus we did not test Ad-B-based constructs for further analyses. Other cpGFP-Ad-A and C constructs (L1-11) showed co-localization with F-actin stained with phalloidin-Atto565 in Hela cells, similarly to the cells expressing their corresponding flex controls (Figure S1B).

Next we evaluated the anisotropy of the fluorescence for cpGFP-Ad-A/C constructs in living HeLa cells expressing each construct using FPM with two polarization orientation analysis (Figure 1C). In this two-axis FPM setup, fluorescent molecules are excited with isotropically polarized LED illumination and the emitted fluorescence is split into two orthogonal polarization orientations, namely 0° (horizontal) and 90° (vertical) (Nakai et al., 2019). For the analysis, horizontal and vertical components are pseudo-colored with green and magenta, respectively. The hue of the pseudo-color of actin filaments represents the degree of the anisotropy of fluorescence. We found that six Ad-A-based constructs, namely L5-10, showed strong green/magenta color. The orientations of fluorescence polarization for these constructs were parallel to the axis of the actin filaments.

To quantitatively analyze the anisotropy of fluorescence of the constructs, we observed the anisotropy of fluorescence at the cortex of prometaphase-arrested HeLa M cells expressing each construct. We defined the polarization value, PV, for evaluation of the degree of anisotropy of fluorescence (see Materials and Methods and Figure S2A for details). cpGFP-Ad-A L5 and 10

showed higher PV values (the absolute value of PV > 0.2) than those of other constructs (Figures 1D and S2B). These results were further confirmed by the analysis using the instantaneous FluoPolScope (Mehta et al., 2016), which instantaneously reports the absolute 2D orientation of fluorescence polarization (Figure S2C and D).

Next we determined the absolute polarization orientation and the anisotropy of fluorescence (polarization factor; see a previous report (Mehta et al., 2016) for more details) of single cpGFP-Ad-A L5 and L10 particles bound to F-actin *in vitro*. The probes with high polarization factor and small variance in the polarization orientation histograms are preferable for studying the 3D architectural dynamics of actin filaments, such as actin network in lamellipodia during the retrograde flow. Recombinant proteins of cpGFP-Ad-A/C constructs were sparsely labeled with actin filaments and analyzed using instantaneous FluorPolScope (Figure 1E and F). Alexa Fluor 488 Phalloidin (AF488-phalloidin) that is known to show high anisotropy of fluorescence when bound to F-actin filaments (Mehta et al., 2016) was used for comparison. The polarization factor for cpGFP-Ad-A L5 was higher than that of L10, similarly to that of AF488-phalloidin. The distribution of the orientation histogram obtained for L5 was as narrow as that of AF488-phalloidin, while the orientation histogram for L10 showed broader distribution (Figure 1E). We could observe the local orientation and the dynamics of actin network during the retrograde flow in the lamellipodia of *Xenopus* tissue culture (XTC) cells expressing cpGFP-Ad-A L5 (movie S1). Thus, we found cpGFP-Ad-A L5 as the best orientation probe for monitoring the orientation of F-actin *in vitro* and in living cells, and hereinafter call it POLArIS^{act}.

Structure determination of POALrIS^{act}

The structure of POLArIS^{act} was determined at 2.5-Å resolution by X-ray crystallography (Figure 1G). We used T57S mutant (residue 57 in cpGFP corresponds to residue 65 in the original avGFP) of POLArIS^{act} because we could not obtain the crystal of original POLArIS^{act} protein suitable for structure determination, possibly due to the peptide-bond cleavage known as "backbone fragmentation", during chromophore formation or maturation (Barondeau et al., 2006) (for details, see Figure S3). No apparent difference was reported in the structure and orientation of chromophores of avGFP and S65T-avGFP (Brejc et al., 1997), thus the T57S mutant is supposed to have the same structure as that of the original POLArIS^{act}.

Remarkably, the 3_{10} helix at the C-terminus of cpGFP was reorganized to an α-helix (Figure 1B and G). The new α-helix was continuously linked to the N-terminal α-helix of Ad-A to form a long α-helix, thereby achieving the constrained tagging. Ligand-binding loops and cpGFP were distantly located, therefore linked cpGFP is unlikely to interfere with the binding of Ad-A to actin filaments. The longitudinal axis of the chromophore was positioned almost perpendicularly to the long axis of the connecting α-helix (Figure 1G, inset).

POLArIS^{act} preferentially binds to F-actin in vitro and in living cells

To investigate the binding property of POLArIS^{act} for F-actin, we performed the co-sedimentation assay with F-actin. We found that POLArIS^{act} binds to F-actin with about 1:1 stoichiometry and with dissociation constant (K_d) of 0.32 ± 0.18 μM (Figures 2A and S4A). Pull-down experiments indicated that POLArIS^{act} has a clear preference for F-actin to G-actin, as its binding to G-actin was undetectable in the assay (Figures 2B and S4B).

The intracellular localization of POLArIS^{act} was re-investigated by co-staining with phalloidin-Atto565 in fixed cells using high-magnification objective lens instead of low-

magnification lens we had used for the screening (Figure S1B). The striking resemblance between their localization (Figure 2C) proved the specific binding of POLArIS^{act} to F-actin in cells.

Next we expressed POLArIS^{act} in living LLC-PK1 cells and compared its localization with exogenously expressed actin (ACTB), Lifeact, UtrCH, or F-tractin. The distribution of POLArIS^{act} was most similar to that of UtrCH, and POLArIS^{act} showed the clearly lower cytoplasmic/nuclear background than ACTB, Lifeact, or F-tractin (Figure 2D). As far as we have tested, POLArIS^{act} labels all F-actin structures that can be labeled by other F-actin probes with the relatively low preference for lamellipodia (Figure 2E). These results demonstrate that POLArIS^{act} can be used as an excellent F-actin marker in living cells. It is worth noting that all cell lines we tested including HeLa, HEK293, LLC-PK1, and Jurkat, grew as normally as the cells without expressing POLArIS^{act}, unless POLArIS^{act} was overexpressed (Figure 2F shows an example of HeLa).

Validation of two-axis FPM observation with POLArIS^{act} using living starfish oocytes

We applied POLArIS^{act} to real-time two-axis FPM imaging of actin dynamics in living starfish eggs to test if physiological actin dynamics can be observed in living samples. Drastic and dynamic changes in F-actin organization in starfish have been reported during oocyte maturation and fertilization (Hamaguchi et al., 2007; Lénárt et al., 2005; Mori et al., 2011, 2014; Santella et al., 2018; Wesolowska et al., 2020). We expressed POLArIS^{act} in starfish oocytes by microinjection of mRNA and monitored their early development processes with two-axis FPM.

First, we focused on the F-actin dynamics during the breakdown of the germinal vesicle (GV) (Figure 3A and movie S2). Before GV breakdown, almost no fluorescence of POLArIS^{act} was

observed on the GV membrane (Figure 3A, 0 min). Approximately 30 min after 1-methyladenine (1-MA) treatment inducing GV breakdown, F-actin was abruptly accumulated on the GV membrane with no apparent fluorescence polarization (5.5 min). Shortly after the F-actin accumulation, the GV started to shrink showing the pseudo-color with green color in top/bottom regions and magenta in right/left (8 min). A transient accumulation of F-actin on the nucleoplasmic side of GV membrane was previously observed during the initial phase of GV breakdown, called F-actin shell (Mori et al., 2014; Wesolowska et al., 2020). F-actin shell was reported to have two components: actin filaments running parallel to GV membrane forming a "base" of the shell, and filopodia-like spikes that protrude perpendicularly to GV membrane from the base (Wesolowska et al., 2020). As actin filaments in the base are supposed to be distributed in nearly 2D, filaments running in the optical plane mainly contribute to the ensemble fluorescence polarization detected by FPM. Thus the fluorescence of POLArIS^{act} bound to actin filaments of the base is supposed to have the polarization orientation parallel to the GV membrane, while fluorescence polarization from spikes is supposed to have the opposite orientation (schematics in insets in the top row, 5.5 and 8 min). The apparent absence of fluorescence polarization (5.5 min) is consistent with the supposition of mixed orientations of fluorescence polarization in the F-actin shell (inset, 5.5 min), as the base and spikes were observed as distinct structures only with high-resolution imaging such as confocal laser scanning microscopy (CLSM) (Mori et al., 2014). The green color in top/bottom regions of GV and magenta in right/left (8 min) suggests that actin spikes were very transient and only the base was remaining.

Subsequently to the disappearance of F-actin shell, meshwork-like F-actin network (Lénárt et al., 2005; Mori et al., 2011) was observed with fluorescence polarization of POLArIS^{act} (Figure 3A, 20 min, arrowheads). The fluorescence signal was gradually weakened with time (34.5 min).

Following the process of GV breakdown, the polar body (PB) was extruded (Figure 3B and movie S3). POLArIS^{act} signal began to be enriched on the cortex near the animal pole (Figure 3B, 0-2 min, arrow). The PB appeared at the animal pole immediately after the F-actin accumulation (2 min, arrowhead). POLArIS^{act} signal rapidly decreased while a half of the PB appeared on the membrane (5-6.5 min) and disappeared as the PB extrusion completed (8-20 min). In Figure 3B, POLArIS^{act} signal was clearly observed as magenta by two-axis FPM, indicating that actin filaments are aligned parallel to the division plane. This is consistent with the proposed model of the contractile ring formation during the PB extrusion (Hamaguchi et al., 2007).

Next we monitored the F-actin dynamics associated with fertilization (Figure 3C-E). We found that a bright POLArIS^{act} signal appeared on the cell surface where sperm entered (Figure 3C, 0 min). From there, an actin-based structure grew into the oocyte (2-8 min) similarly to the previous observations of actin-based structures associated with fertilization (Santella et al., 2018). The strong anisotropy detected with two-axis FPM indicates that this structure was composed of bundles of well-aligned actin filaments. The tip of the bundle, typically reaching about 40 μm from the membrane (Figure 3E), had been connected to the sperm nucleus in the cytoplasm until the nucleus stopped moving in the cytoplasm (Figure 3D and movie S4), which was reminiscent of actin-based motilities of bacterial pathogens (Lamason and Welch, 2017). From these observations, we concluded that our two-axis FPM setup using POLArIS^{act} can

distinguish F-actin assemblies from randomly oriented F-actin accumulations in living starfish eggs and zygotes.

Formation of radially extended actin filaments during mitosis in early embryos of starfish

We next observed F-actin dynamics during the early development of starfish embryos. Observations of F-actin dynamics were supposed to be infeasible with microinjection of fluorescent phalloidin, since it was reported that cleavages and early development of echinoderm embryos are sensitive to phalloidin due to its strong F-actin stabilization effect (Hamaguchi and Mabuchi, 1982). Unexpectedly, we found in the observation of two-axis FPM that the green (horizontal)/magenta (vertical) cross patterns appeared during cleavages (Figure 4A, second and third rows, and movie S5). The visibility of the cross patterns was further enhanced by using the differential images of horizontal/vertical polarization (Figure 4A, fourth row). Two small cross patterns appeared near the center of the zygote (Figure 4A, 20 min) and rapidly expanded and reached cell surface before the ingression occurred (24 min). The cross patterns persisted during the cleavage (39-56.5 min) and disappeared when the cleavage finished (59 min). We had similar observations repeatedly in every cleavage, even in later developmental stages (Figure 4B and movie S6).

To evaluate the changes in the local distribution of the cross-patterns, we deduced the center of the cross pattern from the differential polarization image by image analysis, set concentric circular shells around the deduced center of the cross pattern, and plotted the autocorrelation as the circular shell is rotated around the center (see Materials and Methods for details). A cross pattern should result in high autocorrelation when rotated by π (peak) and low autocorrelation when rotated by $\pi/2$ or $3\pi/2$ (troughs). The amplitude (the difference between the peak and the

troughs) becomes higher when the cross pattern is more evident. The analyses clearly showed the dynamic appearance and disappearance of cross patterns during cleavages (Figure 4A, bottom row, rotation auto-corr.).

The observation above implies the appearance and disappearance of actin filaments radially aligned from two centers in wide 3D range during the cleavages. To confirm the presence of radially aligned actin filaments, we observed fixed eggs with conventional CLSM. As fixatives based on paraformaldehyde (PFA) or PFA in combination with glutaraldehyde (GA) failed to preserve these F-actin structures in dividing starfish eggs (data not shown), we tried the recently reported glyoxal fixation (Richter et al., 2018). Although fluorescence of POLArIS^{act} was diminished by glyoxal fixation, two-axis FPM observation of phalloidin-Atto565 staining in a fixed POLArIS^{act}-expressing egg showed the characteristic cross pattern as we had observed in live starfish embryos (Figure 4C, left 3 panels). Using CLSM, radially extending actin filaments were certainly visible in the same egg (Figure 4C, right panel). The observation of similar radial distribution of F-actin in eggs without injection of POLArIS^{act} mRNA (Figure 4D) excluded the possibility of artifacts caused by the expression of POLArIS^{act}.

We next compared the distribution of F-actin and microtubules in a fixed starfish embryo expressing POLArIS^{act} in the first cleavage (Figure 5A). CLSM observation visualized numerous actin filaments extended from two points. Staining with α-tubulin antibody indicated that these two points were centrosomes. Similar distributions of F-actin and microtubules were also observed in the third cleavage (Figure 5B). Compared with microtubule-based asters, F-actin staining seemed to have a more intricate i.e. “fluffy” texture. From these results, we named this structure as FLARE (FLuffy And Radial actin-aster associated with mitosis in Embryo). To our

best knowledge, no report has demonstrated the presence of this structure made of F-actin *in vivo*.

Dynamics of FLARE is tightly associated with that of microtubule aster

We next carried out live-cell observation of FLARE with microtubules visualized with EMTB-mCherry (Miller and Bement, 2009) (Figure 5C and movie S7). With EMTB-mCherry, microtubule asters were observed as widespread staining of mCherry rather than radially aligned microtubules (Figure 5C, contours of asters were indicated by white dashed lines). FLARE and microtubule aster appeared at the same time, expanded at the similar speed, and disappeared simultaneously. Before cleavage initiation, EMTB-mCherry fluorescence was concentrated around two points corresponding to centrosomes (indicated by asterisks, see Figure 5D for details). EMTB-mCherry fluorescence was also detected between centrosomes, which corresponds to a mitotic spindle. Very weak and tiny cross patterns of FLARE were observed around these points (Figure 5C, 0 min). Concentrated fluorescence of EMTB-mCherry gradually became faint and spread as the cross patterns of FLARE expanded (8 min). The front of the expanding EMTB-mCherry fluorescence and the cross pattern of FLARE reached cell surface at 12 min, stayed during the cleavage (16-20 min), and finally, mCherry fluorescence was localized only at two centers and the cross patterns became very weak and small when division finished (36 min). These synchronized dynamics of microtubules and F-actin were also observed in the later cleavages of the same embryo and all other embryos co-expressing POLArIS^{act} and EMTB-mCherry that we observed (data not shown).

Dynamics and maintenance of FLARE are microtubule-dependent

As described above, the dynamics and the distribution of FLARE are very similar to those of microtubule aster. To test the possible interdependence between FLARE and microtubule aster, we carried out pharmacological experiments. First, we used cytochalasin D, the actin polymerization inhibitor (Figure S5). Treatment of a starfish embryo with cytochalasin D resulted in the loss of FLARE formation, while microtubule aster still showed the repeated dis- and re-appearance, indicating that microtubule aster dynamics is not dependent on FLARE.

Next, to examine if the microtubule aster plays a role in the formation and/or the maintenance of FLARE, we treated starfish embryos with microtubule polymerization inhibitor nocodazole (NCZ) at different time points. When NCZ was added to the embryos immediately after microtubule asters started to extend, both microtubule asters and FLARE stopped expanding (Figure 6A, 0-1 min). EMTB-mCherry fluorescence and FLARE polarization gradually disappeared (2-11 min) and the embryo failed to complete the cleavage (18-46 min). Thereafter, cleavages did not occur, and neither the microtubule aster nor FLARE reappeared in the same embryo. These observations indicate that the expansion of the microtubule aster is a prerequisite for the FLARE formation. Next we treated an embryo with NCZ after microtubules sufficiently extended throughout cytoplasm. In this case, microtubule aster was depolymerized outwardly from its center and the fluorescence polarization of FLARE disappeared simultaneously (Figure 6B, 1’45”-4’45”), indicating that the maintenance of FLARE requires the integrity of the astral microtubules. These results demonstrate that both the formation and the maintenance of FLARE depend on the dynamics of microtubules and the integrity of the microtubule aster.

FLARE formation is not Arp2/3 complex dependent

Arp2/3 protein complex and formin family proteins are known as major actin nucleation factors (Amann and Pollard, 2001; Pruyne et al., 2002). We attempted to determine which factor is responsible for the formation of FLARE by pharmacological inhibition of the activity of Arp2/3 complex and formins with CK666 (Nolen et al., 2009) and SMIFH2 (Rizvi et al., 2009), respectively. Since SMIFH2 turned out to be impermeable to fertilization envelopes (Figure S6A), we microinjected artificial seawater containing SMIFH2 under the elevated fertilization envelopes and perfused SMIFH2 directly to eggs (Figure S6B). We unexpectedly found that not only actin but also microtubules lost their dynamics (10-30 min) and eggs failed to divide at various concentrations of SMIFH2 (Figure S6B and data not shown). This implies that SMIFH2 might have nonspecific side effect(s) in starfish eggs other than formin inhibition, so we could not determine if formin family proteins are involved in the formation of the FLARE in our preparations.

When embryos were treated with CK666 immediately after the first cleavage (Figure 7), subsequent cleavages did not occur but microtubule aster showed repeated dis- and re-appearance, confirming that CK666 specifically inhibited Arp2/3-dependent actin nucleation and thereby prevented eggs from dividing without affecting microtubule dynamics. FLARE also appeared and disappeared repeatedly, indicating that Arp2/3 is not essential for the FLARE formation.

Discussion

Our previous studies on cytoskeletal dynamics (Terada et al., 1996, 2000) have led us to focus on fluorescence polarization techniques, as the polarized fluorescence might enhances the sensitivity of fluorescence microscopy for detecting the initial phase of polymerization when the

cytoskeletal protein molecules do not form filaments. Through the years of our trials to use FPM to cytoskeletal proteins, we noticed that the biggest challenge was the difficulty in constrained tagging of each protein of interest with fluorescent proteins. Designing more versatile and affordable methods were required for the constrained tagging of fluorescent labels to any biomolecules of interests. We addressed this task by using a small recombinant binder protein against a specific target of interest, obtainable by phage-display screening, as a scaffold to connect target molecules with circularly permutated sfGFP. As described in this report, we succeeded in establishing a new tool, POLArIS. We expect that POLArIS will spread fluorescence polarization techniques in biomedical research as the users can avoid the difficulty in the constrained tagging. It is worth noting that nucleic acids or lipids can be target molecules of POLArIS in addition to proteins.

Here, by using POLArIS^{act}, the first POLArIS example, we show that POLArIS can report the orientation and localization of F-actin in living cells. The observation of starfish eggs and embryos expressing POLArIS^{act} with FPM revealed a newly identified structure, FLARE. We found no indication of the existence of ordered structures with conventional fluorescence observations, but with FPM and POLArIS^{act}, the presence of radially orientated actin filaments was apparent by their polarized fluorescence. This is reminiscent of Shinya Inoué's first visualization of mitotic spindle dynamics in living cells using polarization microscope in 1950s, which could not have been achieved with conventional microscopic techniques of the time (Inoué, 1953, 1981).

The discovery of FLARE was an unexpected result, as the cytoskeletal organization in starfish embryos had been extensively investigated. There are three major possibilities why FLARE had been left from its discovery until today. First, starfish embryos have the very high cytoplasmic

autofluorescence which strongly disturbs the live imaging using fluorescent proteins. Second, traditional fixatives including PFA and GA seem unable to preserve FLARE structure efficiently. We found glyoxal was suitable for fixing actin filaments in FLARE. It was reported that immunostaining of glyoxal-fixed neurons with anti-β-actin antibody showed a significantly brighter staining than that of PFA-fixed neurons (Richter et al., 2018). In addition, small molecular size of glyoxal might be advantageous in terms of penetration and diffusion in large (>100 μm in diameter) starfish eggs. Third, high-resolution fluorescence microscopy techniques such as CLSM are suitable to reveal fine structures in relatively small areas, but not suitable for structures distributed in large areas, especially those with rapid dynamics in living biological specimens. In contrast, FPM is supposed to be suitable to reveal orderly arranged structures distributed in large areas, including FLARE.

At present, the mechanism for the FLARE formation and its function remain to be elucidated. Centrosomes isolated from Jurkat cells formed radial F-actin array *in vitro* (Farina et al., 2016), which resembles FLARE, and actin filaments were found to be localized around centrosomes in HeLa and Jurkat cells (Farina et al., 2019; Inoue et al., 2019). Moreover, radially extended actin filaments from centrosomes were observed in HeLa cells during the forced exit of mitosis after prometaphase arrest with *S*-trityl-L-cysteine (Farina et al., 2019). Actin nucleation activity of centrosomes in these examples, however, was reported to require Arp2/3 complex, while FLARE formation was not affected by Arp2/3 inhibition. Thus, it is unlikely that FLARE is intrinsically the same as these F-actin related structures around centrosomes in cultured human cells. Recently, using *Xenopus* egg extract, the formation of radially aligned actin filaments around centrosomes were observed in thin, two-dimensional space (Field et al., 2019). The authors

mentioned that they failed to preserve F-actin by chemical fixation of *Xenopus* eggs. Glyoxal fixation might help preserve actin filaments in *Xenopus* eggs during cleavages *in vivo*.

All data presented here demonstrate that POLArIS^{act} is an excellent F-actin probe for FPM, in terms of reporting the position and the orientation of F-actin, the high specificity with low background fluorescence, and the low cytotoxicity that allows to follow physiological dynamics of F-actin in living specimens. To date, fluorescently labeled phalloidin has been commonly used as an F-actin probe for FPM, but its strong F-actin stabilizing effect is not preferable for physiological studies in live cells. The successful application of POLArIS^{act} to study the dynamics of actin cytoskeleton during the early development of echinoderm eggs which was reported to be too sensitive to be explored with fluorescent phalloidin (Hamaguchi and Mabuchi, 1982), strongly suggests that POLArIS^{act} is a promising alternative to fluorescent phalloidin for F-actin studies in living cells with FPM.

Polarization is one of the most basic and fundamental properties of light. Our method will open a new avenue to various fluorescent spectroscopic applications such as, but not limited to, high throughput screening, super-resolution, resonance energy transfer, and fluorescence correlation. By taking advantage of the genetically encoded nature, POLArIS has a potential of supporting broader applications of fluorescence polarization techniques to a variety of cell types, species, and many types of specimens such as developing tissues and whole animals.

Acknowledgments

We are grateful to N. Nakai (TMDU) and H. T. Miyazaki (NIMS) for helpful discussion, O. Hoshi (TMDU) for continuous encouragement, and to M. Taguchi (TMDU) for secretarial and experimental assistance. We deeply thank H. Iwasaki (Gunma-U) for suggestion making the

initial opportunity of the collaborative research using starfish oocytes, R. Nitta and M. Aoki (RIKEN) for discussion and initial trial for the crystallization of POLArIS^{act}, K. Hanada and M. Inoue (RIKEN) for plasmid preparation for the expression of POLArIS^{act} protein in bacterial cells, and T. M. Watanabe (RIKEN-QBiC) for discussion and initial assistance for FPM construction. We are grateful to the late Dr. Shinya Inoué (1921 - 2019), the father of polarized light microscopy, for his great support and his pioneering work of polarized fluorescence in green fluorescent protein crystals (Inoué et al., 2002). **Funding:** Japan Society for the Promotion of Science (JSPS) Grant-in-Aid for Scientific Research (KAKENHI) (C) and (B) (18K06819 to Kei.S., 17K07405 to K.C., 17H04013, 26293038 to S.T.); Fostering Joint International Research (B) (18KK0222 to S.T.); JSPS Bilateral Joint Research Projects (Open Partnership Joint Research Projects) (1006285 to S.T.); Takeda Science Foundation to K.C.; National Institutes of Health (R01 GM100160 to T.T.); MBL Telfer Fund to T.T.; Platform Project for Supporting Drug Discovery and Life Science Research (Basis for Supporting Innovative Drug Discovery and Life Science Research (BINDS)) from AMED (JP19am0101082 to M.S.).

Author Contributions: Discussion with T.T. led S.T. to start a close collaboration with T.T. and to conceive of the project. A.S. and Kei.S. conducted most experiments and performed analysis with other collaborators. K.C. performed injections into starfish oocytes and supervised the related experiments. Kei.S. and Ken.S. jointly constructed the two-axis FPM along with the guidance by T.T. M.K. contributed imaging analysis for starfish embryo data. S.M. contributed instantaneous FluoPolScope analysis tools. Y.T. worked with N.S. to collect the crystallography data and determined structures under the supervision by M.S. T.T. conducted experiments and performed analysis by instantaneous FluoPolScope with assistance of H.I. S.T. designed

experiments and supervised the project. A.S. and Kei.S. jointly wrote the manuscript with inputs from all authors.

Declaration of Interests: The authors declare no competing interests.

Materials Availability: Plasmids generated in this study will be deposited to Addgene or will be made available upon reasonable request.

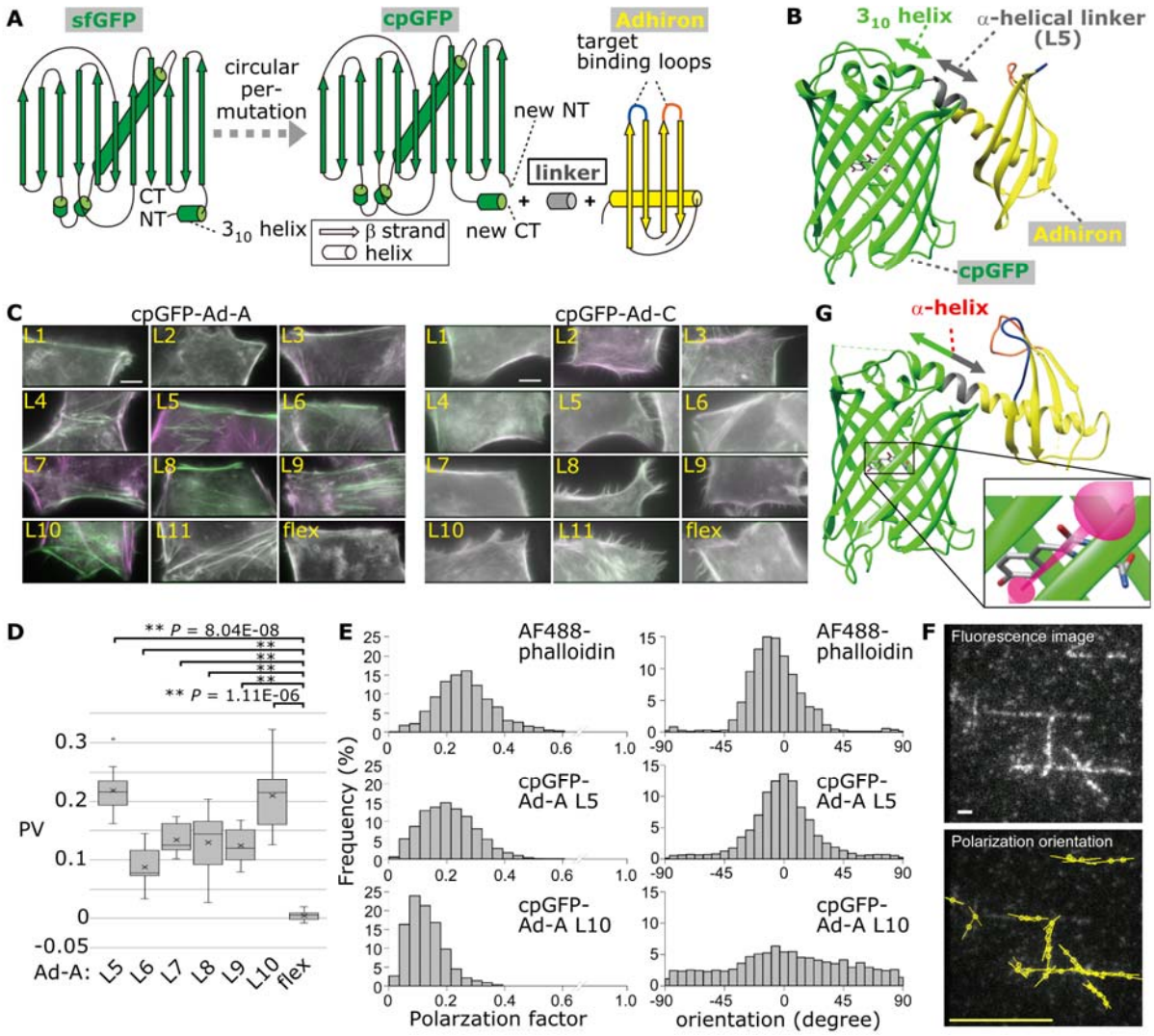

Figure 1. Design of POLArIS and development of POLArIS^{act}.

(A) Schematic of the circular permutation of sfGFP to create cpGFP, and fusion of cpGFP and Adhiron with a linker.

(B) Modeling of cpGFP-Adhiron (L5) structure with UCSF Chimera.

(C) Two-axis FPM images of HeLa cells expressing cpGFP-Ad-A/C constructs. Horizontal and vertical components are shown in green and magenta, respectively. Scale bar: 10 µm.

(D) PVs of indicated cpGFP-Ad-A constructs are shown by boxplots with mean values (cross marks). Statistics: Student's t-test with Šidák correction. **, $P < 0.01$. n=10.

(E) *In vitro* evaluations of cpGFP-Ad-A L5/L10 by particle analysis with instantaneous FluoPolScope. Histograms of the polarization factor (left) and polarization orientation (right) for Alexa Fluor 488 phalloidin (top), cpGFP-Ad-A L5 (middle) and L10 (bottom). Orientation at 0° and ±90° indicates the polarization orientation of the particle is parallel and perpendicular, respectively, to actin filaments.

(F) Representative images of instantaneous FluoPolScope analysis of cpGFP-Ad-A L5. Top: fluorescence image. Bar, 1 µm. Bottom: polarization orientations. Length of bars represent the polarization factor. Yellow bar: polarization factor = 0.5.

(G) The crystal structure of POLArIS^{act} (T57S). Magenta two-way arrow: presumed orientation of the dipole of cpGFP (depicted according to (Rosell and Boxer, 2003)).

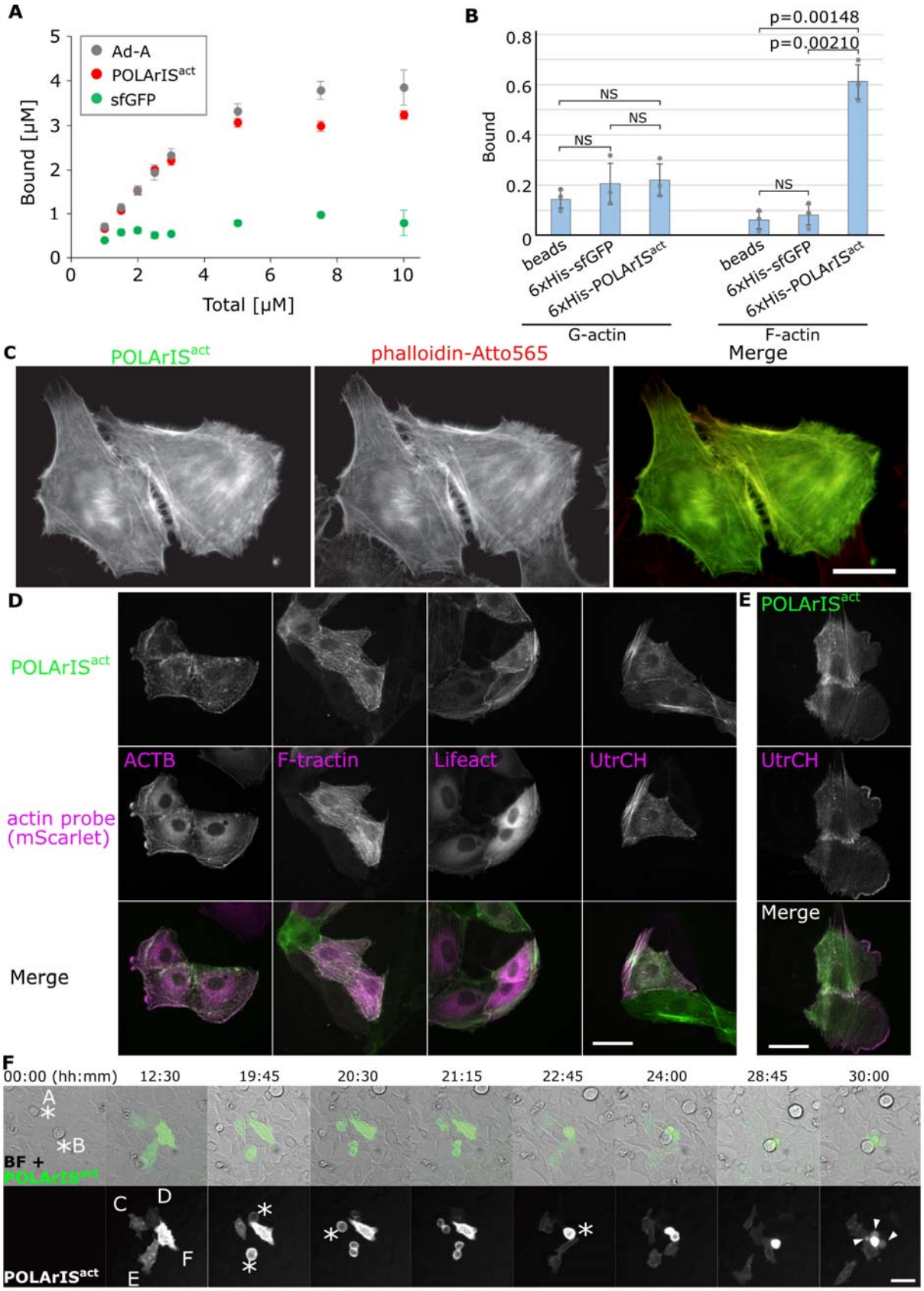
A
Ad-A
POLArIS^act
sfGFP
Bound [μM]
Total [μM]
B
p=0.00148
p=0.00210
NS
Bound
beads
6xHis-sfGFP
6xHis-POLArIS^act
G-actin
F-actin
C
POLArIS^act
phalloidin-Atto565
Merge
D
POLArIS^act
ACTB
F-tractin
Lifeact
UtrCH
actin probe (mScarlet)
Merge
E
POLArIS^act
UtrCH
Merge
F
00:00 (hh:mm)
12:30
19:45
20:30
21:15
22:45
24:00
28:45
30:00
BF + POLArIS^act
POLArIS^act

Figure 2. Properties of POLArIS^{act} as an F-actin probe

(A) Plots of the mean values in co-sedimentation assays with F-actin were shown for Ad-A (gray), sfGFP (green) or POLArIS^{act} (red) with error bars showing standard deviations. Data were from three independent experiments.

(B) The mean values of the bound fraction in pull-down assays were shown for G- or F-actin with error bars showing standard deviations. *P* values were calculated by applying Šidák multiple comparison correction to Student's t-test. Data were from three independent experiments. Gray circles indicate the values from individual experiments.

(C) High-resolution images of fixed HeLa cells expressing POLArIS^{act} stained with phalloidin-Atto565. Scale bar: 20 µm.

(D and E) Comparison of the localization of POLArIS^{act} with ACTB and other F-actin probes tagged with mScarlet in living LLC-PK1 cells. POLArIS^{act} showed the low background compared to ACTB, F-tractin, and Lifeact, similarly to UtrCH (D), with the lower preference for lamellipodia than UtrCH (E). Scale bars: 50 µm.

(F) Live-cell time lapse imaging of HeLa cells transfected with POLArIS^{act} plasmid. Cells A and B in mitosis at time 0 (soon after transfection) divided to cells C and D, E and F, respectively, then expressed POLArIS^{act} (time 12:30). The order of expression level was: F>E>C>D. While cells C, D, and E divided successfully, cell F failed to divide and died forming blebs (time 30:00). Asterisks indicate cells in mitosis; arrowheads indicate blebs. Scale bar: 50 µm.

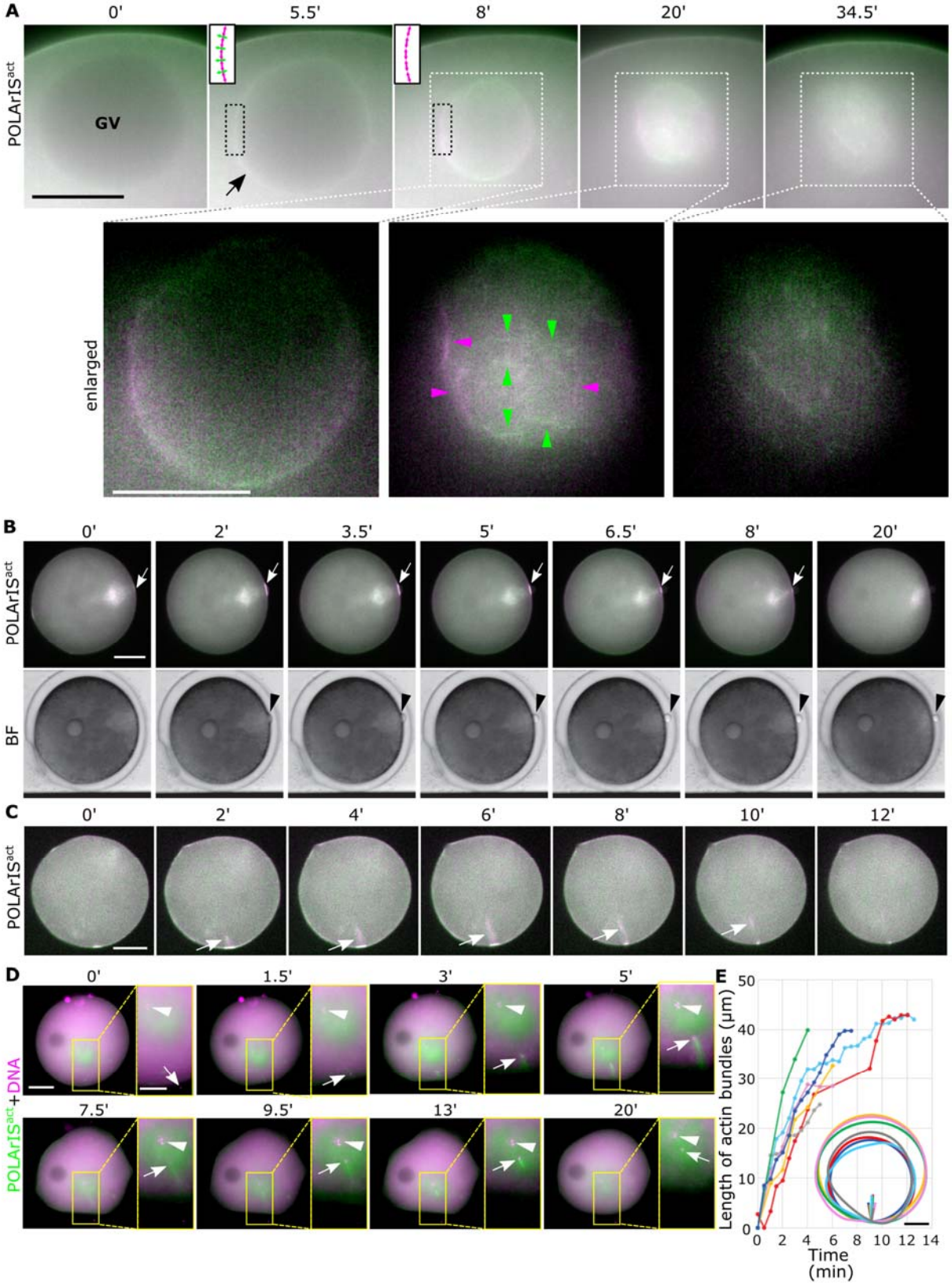
A
0'
5.5'
8'
20'
34.5'
POLArIS^{act}
GV
enlarged
B
0'
2'
3.5'
5'
6.5'
8'
20'
POLArIS^{act}
BF
C
0'
2'
4'
6'
8'
10'
12'
POLArIS^{act}
D
0'
1.5'
3'
5'
7.5'
9.5'
13'
20'
POLArIS^{act}+DNA
E
Length of actin bundles (μm)
Time (min)

Figure 3. FPM observation of GV breakdown, PB extrusion and fertilization of starfish oocytes expressing POLArIS^{act}.

(A) Time lapse images of two-axis FPM of starfish oocytes expressing POLArIS^{act} during GV breakdown. Time 0 is just before the breakdown, approximately 30 min after 1-MA addition. Regions marked by white dashed line boxes are magnified in the bottom panels (enlarged). An arrow indicates the "F-actin shell". Arrowheads in bottom row indicate actin filaments with clear polarization in the meshwork (green: horizontal, magenta: vertical). Two-way-arrows in insets in the top row schematically indicate supposed orientations of fluorescence polarization of POLArIS^{act} bound to local F-actin structures (green, base of the shell; magenta; spikes) in regions marked by black dashed line boxes. In bottom panels, background signal was subtracted for the better presentation of actin meshwork.

(B) Time lapse images of starfish oocytes expressing POLArIS^{act} during the PB extrusion with two-axis FPM (top panels) and bright field view (bottom panels). Arrowheads indicate the polar body and arrows indicate contractile ring-like F-actin, respectively.

(C) Time lapse two-axis FPM images of a starfish oocyte expressing POLArIS^{act} during fertilization. Arrows indicate actin bundles associated with fertilization. Scale bars: 25 µm (A), 50 µm (B and C).

(D) Time lapse fluorescence microscopy images of starfish oocyte expressing POLArIS^{act} (green) with Hoechst staining (magenta). Areas enclosed by yellow boxes in left panels are magnified in right panels. In some right panels, background signal was subtracted for better visibility. After fertilization, sperm DNA (arrows) was positioned at the tip of the actin bundle until it stopped moving (3-13 min). The actin bundle was gradually depolymerized (9.5-13 min), and finally disappeared (20 min). Interestingly, after the extension of the actin bundle, the sperm

DNA and the egg DNA (arrowheads) were closely apposed (9.5-20 min), as if the sperm DNA was conveyed to the egg DNA by the extension of the actin bundle. Scale bars: 50 µm (left), 25 µm (right).

(E) Plots of the length of actin bundles over time in different colors for each oocyte (n = 8). Actin bundles typically extended perpendicularly to the cell surface and reached about 40 µm deep. The schematic shows the trajectory of the actin bundle in each egg and the outline of the same egg, with the same color as that of plot graph. Scale bar: 50 µm

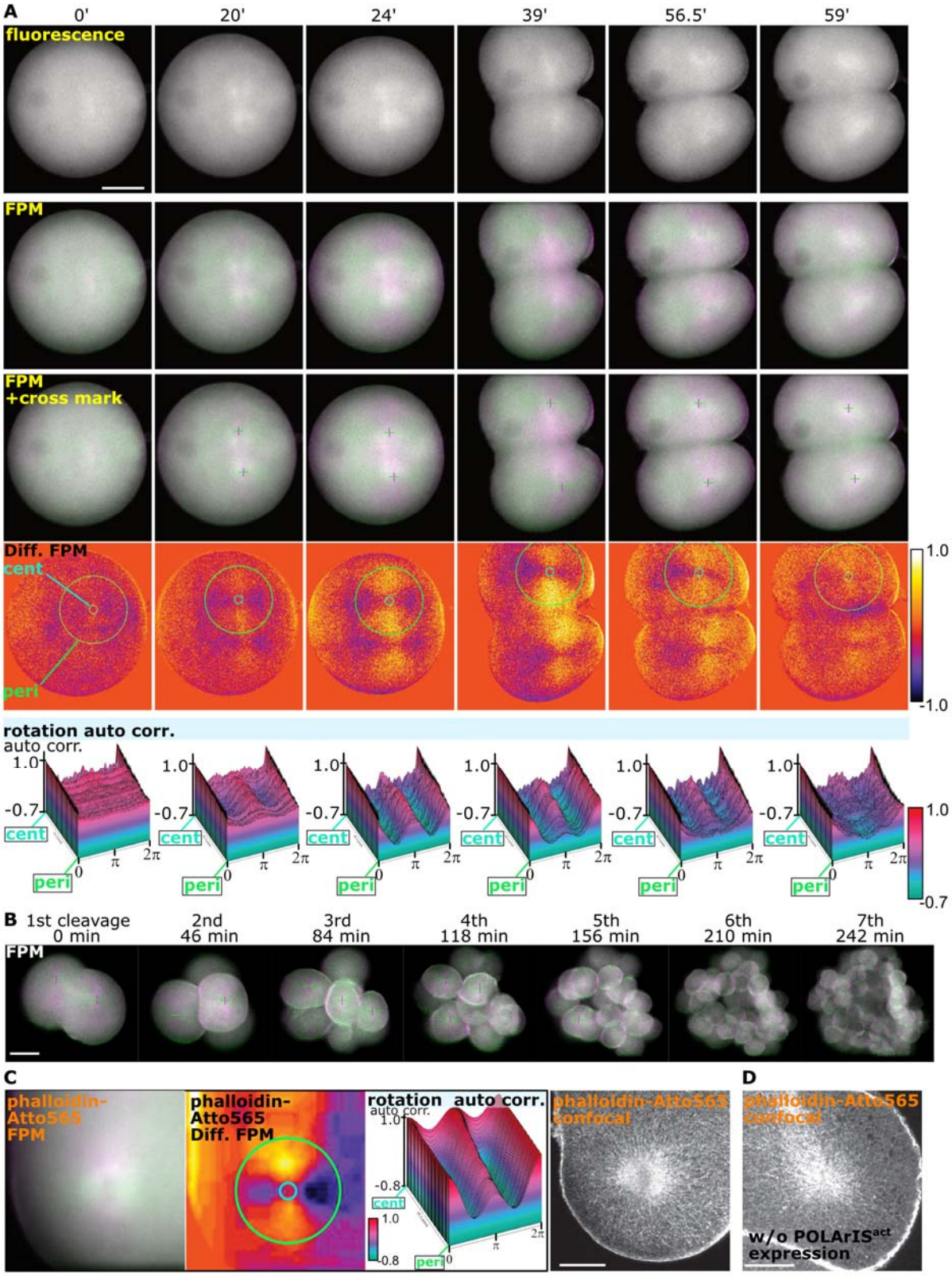
A
0'
20'
24'
39'
56.5'
59'
fluorescence
FPM
FPM
+cross mark
Diff. FPM
cent
peri
1.0
-1.0
rotation auto corr.
auto corr.
1.0
-0.7
cent
peri
0
π
2π
1.0
-0.7
B
1st cleavage
0 min
2nd
46 min
3rd
84 min
4th
118 min
5th
156 min
6th
210 min
7th
242 min
FPM
C
phalloidin-
Atto565
FPM
phalloidin-
Atto565
Diff. FPM
rotation auto corr.
auto corr.
1.0
-0.8
cent
peri
0
π
2π
1.0
-0.8
phalloidin-Atto565
confocal
D
phalloidin-Atto565
confocal
w/o POLArIS^act
expression

Figure 4. Organization and dynamics of FLARE during starfish egg cleavages.

(A) Time lapse images during the first cleavage of a starfish egg expressing POLArIS^{act} with fluorescence microscopy (the top row) and two-axis FPM (green/magenta in second and third rows and differential in the fourth row). Cross marks in the third row indicate the centers of the green/magenta cross patterns. The bottom row shows the 3D-plots of the rotational autocorrelation analyses of green/magenta cross patterns. Light blue circles (annotated as cent for center) and light green circles (annotated as peri for peripheral) in differential images indicate circles of minimum and maximum diameters used in the autocorrelation analyses. Z axis shows the normalized autocorrelation. Scale bar: 50 µm.

(B) Time lapse two-axis green/magenta FPM observation of a starfish embryo expressing POLArIS^{act} from the first to the seventh cleavage. FLARE could not be recognized after the fifth cleavage because of the background signal from blastomeres overlapped in Z-axis direction. Time 0 was set arbitrarily to the frame in which FLAREs were clearly visible during the first cleavage. Scale bar: 50 µm.

(C) Green/magenta (left) , differential (middle left, with circles of min/max diameters used in autocorrelation analyses), 3D-plot of rotational autocorrelation analysis (middle right) of two-axis FPM, and a CLSM (right) image of phalloidin-Atto565 staining of a glyoxal-fixed starfish egg expressing POLArIS^{act} in the second cleavage. Images of FPM and CLSM were taken from the same region with almost the same z-axis planes of the same egg. Scale bar: 25 µm.

(D) CLSM image of phalloidin-Atto565 staining in a non-injected egg during the third cleavage. Regardless of POLArIS^{act} expression, actin filaments of FLARE were observed in fixed starfish eggs. Scale bar: 25 µm.

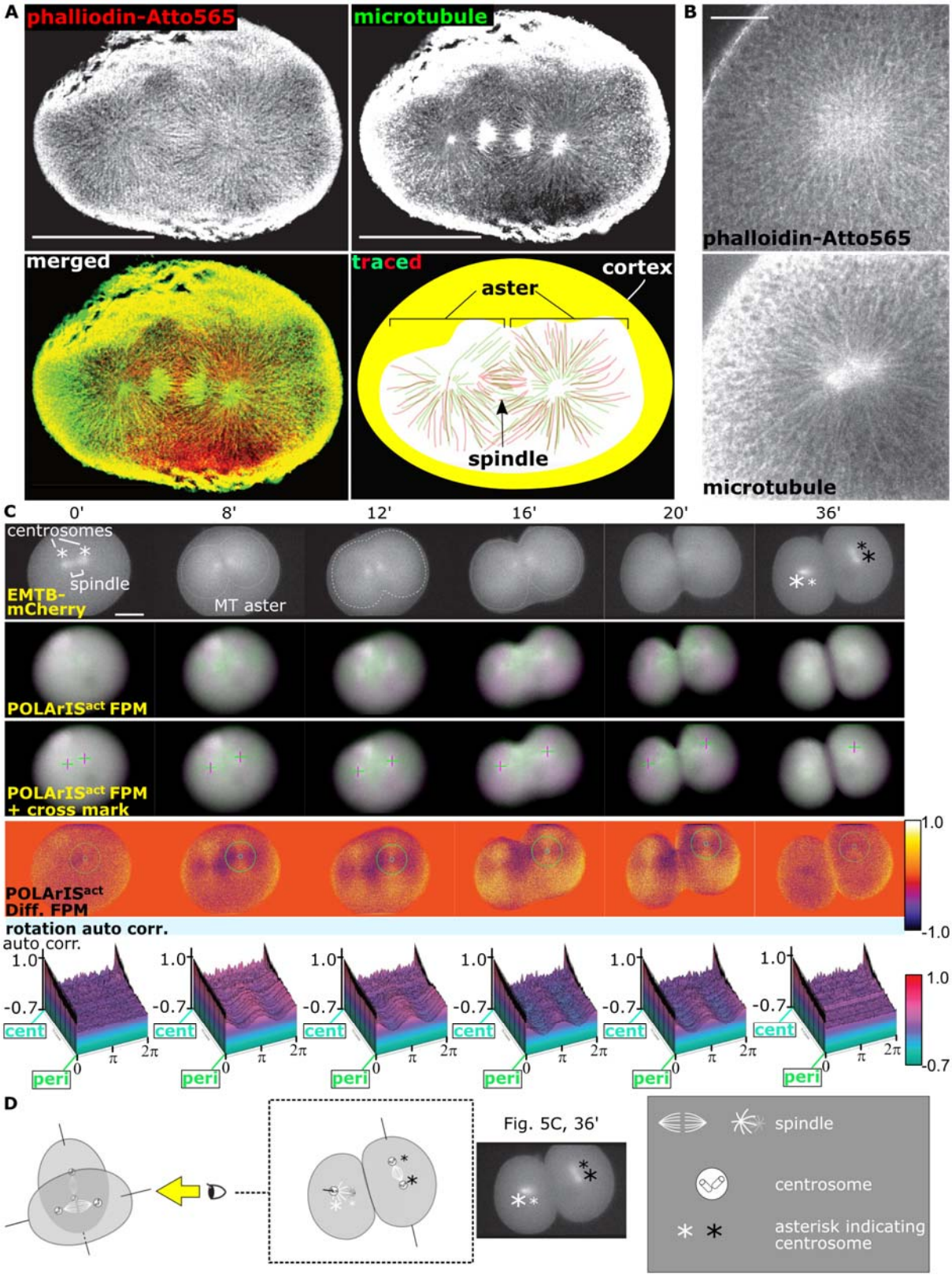
A
phalliodin-Atto565
microtubule
merged
traced
cortex
aster
spindle
B
phalloidin-Atto565
microtubule
C
0'
8'
12'
16'
20'
36'
centrosomes
spindle
EMTB-mCherry
MT aster
POLArIS act FPM
POLArIS act FPM + cross mark
POLArIS act Diff. FPM
1.0
-1.0
rotation auto corr.
auto corr.
1.0
-0.7
cent
peri
0
π
2π
D
Fig. 5C, 36'
spindle
centrosome
asterisk indicating centrosome

Figure 5. Comparisons of the distribution and dynamics of FLARE and microtubule asters.

(A, B) CLSM images of F-actin (phalloidin-Atto565) and microtubules (anti-α-tubulin staining) in glyoxal-fixed starfish embryos expressing POLArIS^{act} in the first (A) and the third (B) cleavages. In the schematic, filaments of actin (red) and microtubule (green) were manually traced from microscopic pictures (A, bottom right). Scale bars: 100 µm (A), 20 µm (B).

(C) Time lapse green/magenta (second and third rows) and differential (fourth row, with circles of min/max diameters in autocorrelation analyses) two-axis FPM images of the first cleavage of a starfish embryo expressing POLArIS^{act} and EMTB-mCherry. Top row shows vertical polarization images of EMTB-mCherry. Cross marks (third row) indicate centers of green/magenta cross patterns. Bottom row shows 3D-plots of autocorrelation analyses of FLARE. Centrosomes are shown by asterisks (see Figure 5D for details). Contours of microtubule asters are shown by dashed lines. In POLArIS^{act} images, background signal was subtracted for better presentation of cross patterns. Scale bar: 50 µm.

(D) Schematic of the arrangement of spindles and centrosomes in the panel of Figure 5C, 36 min. Larger asterisks indicate centrosomes nearer the objective lens. Asterisks with the same color indicate centrosomes in the same blastomere.

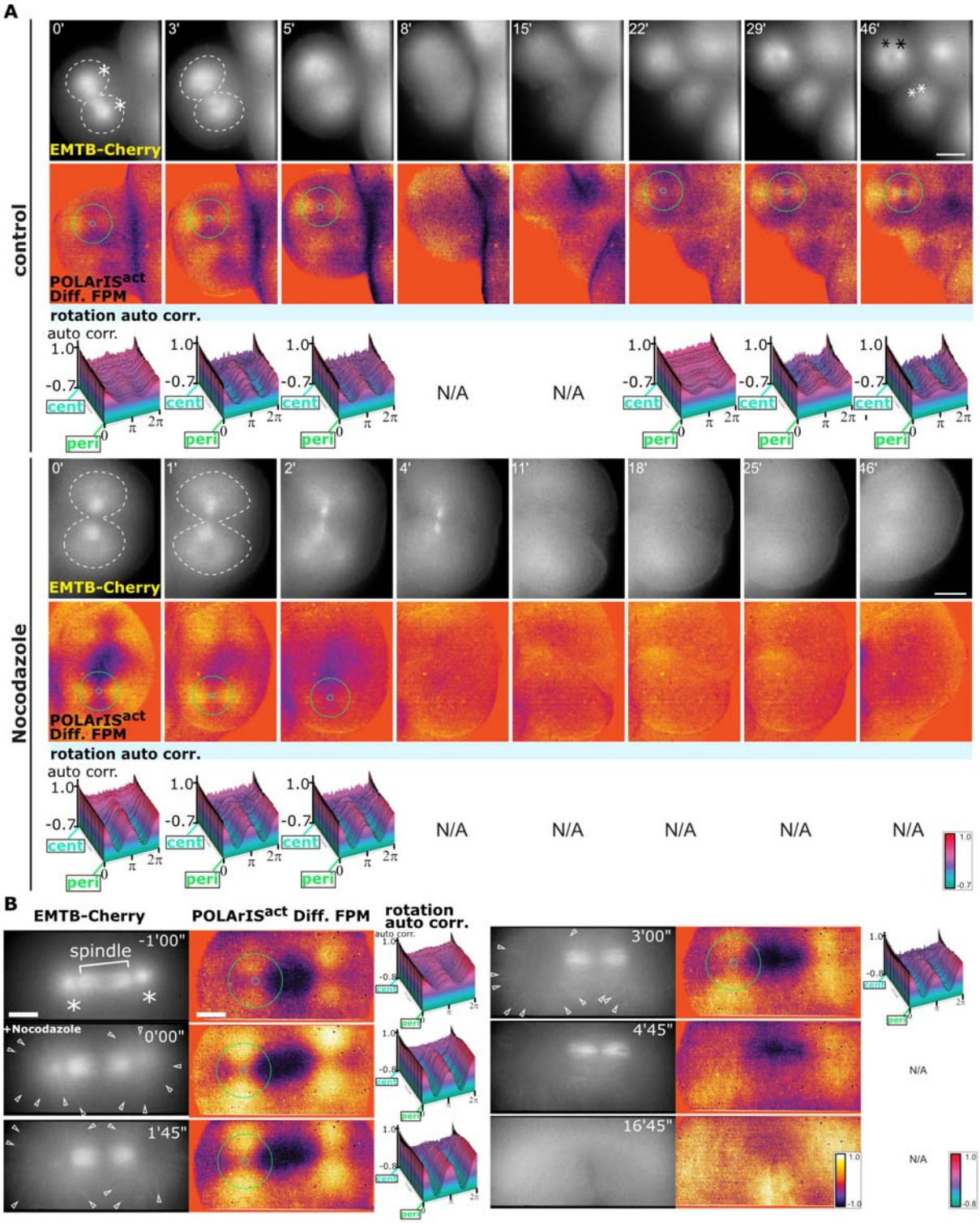
A
control
0'
3'
5'
8'
15'
22'
29'
46'
EMTB-Cherry
POLArIS act
Diff. FPM
rotation auto corr.
auto corr.
1.0
-0.7
cent
peri
0
π
2π
N/A
Nocodazole
0'
1'
2'
4'
11'
18'
25'
46'
EMTB-Cherry
POLArIS act
Diff. FPM
rotation auto corr.
auto corr.
N/A
B
EMTB-Cherry
POLArIS act Diff. FPM
rotation auto corr.
spindle
-1'00"
+Nocodazole
0'00"
1'45"
3'00"
4'45"
16'45"
N/A

Figure 6. FLARE dynamics is disrupted by inhibiting polymerization of microtubules

(A, B) Time lapse two-axis FPM observation of nocodazole-treated eggs expressing POLArIS^{act} and EMTB-mCherry in the fourth (A) and the third cleavages (B).

(A) Top rows show vertical polarization images of EMTB-mCherry (asterisks indicate centrosomes, dashed lines indicate contours of microtubule asters), middle rows show differential FPM images of POLArIS^{act} with circles of min/max diameters used in autocorrelation analyses, and bottom rows show 3D-plots of autocorrelation analyses of FLARE. N/A means that no center of the cross pattern was identified in our search algorithm. Drug was added at time 0. Scale bar: 50 µm.

(B) Left columns show vertical polarization images of EMTB-mCherry (asterisks indicate centrosomes), middle columns show differential FPM images with circles of min/max diameters used in autocorrelation analyses, and right columns show 3D-plots of autocorrelation analyses of FLARE structures. N/A means that no center of the cross pattern was identified in our search algorithm. Drug was added after confirming at least one astral microtubule reached the cell surface (time 0). A silicone immersion 40x objective lens and a 1.5x intermediate magnification lens were used to visualize microtubule filaments (arrowheads). Scale bar: 25 µm.

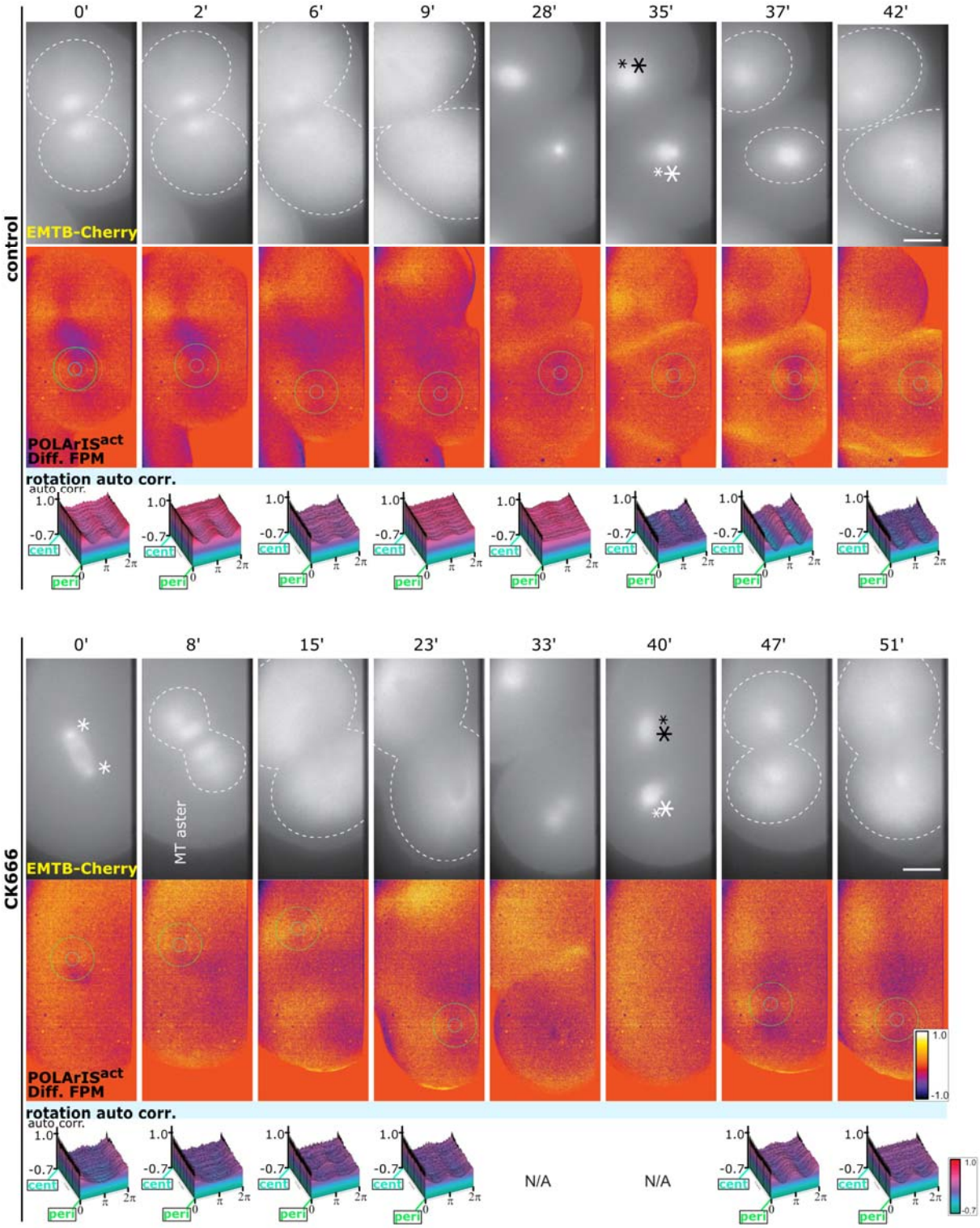
control
0'
2'
6'
9'
28'
35'
37'
42'
EMTB-Cherry
POLArIS act
Diff. FPM
rotation auto corr.
auto corr.
1.0
-0.7
cent
peri
0
π
2π
CK666
0'
8'
15'
23'
33'
40'
47'
51'
MT aster
EMTB-Cherry
POLArIS act
Diff. FPM
1.0
-1.0
rotation auto corr.
N/A
N/A
-0.7

Figure 7. FLARE formation and dynamics are independent of the actin nucleation by Arp2/3.

Time lapse two-axis FPM observations of DMSO (control) or CK666 treated starfish embryos expressing POLArIS^{act} and EMTB-mCherry. Drugs were added immediately after the first cleavage completed (time 0). Top rows show vertical polarization images of EMTB-mCherry (asterisks indicate centrosomes, dashed lines indicate contours of microtubule asters), middle rows show differential FPM images of POLArIS^{act} with circles of min/max diameters used in autocorrelation analyses, and bottom rows show 3D-plots of autocorrelation analyses of FLARE. N/A means that no center of the cross pattern was identified in our search algorithm. Scale bar: 25 µm.

Materials and Methods

Cell culture

HeLa cells (generous gift from Dr. Yoshimori, Osaka University) and HeLa M cells (generous gift from Dr. Lowe, University of Manchester) were incubated at 37°C in Dulbecco's modified Eagle medium (DMEM, nacalai tesque) containing 10% fetal bovine serum (FBS) with 5% CO_2. LLC-PK1 cells (EC86121112-F0, ECACC) were incubated at 37°C in Medium 199 (Merck) containing 10% fetal bovine serum (FBS) with 5% CO_2. XTC cells (generous gift from Dr. Mitchell, Northwestern University) were incubated at room temperature in 70% Leibovitz's L-15 medium (Thermo Fisher Scientific) containing 10% FBS.

Plasmid construction

Sequence information of binding domains of Adhirons used in this study was described at the 60th Annual Meeting of Biophysics Society (Lopata et al., 2016). DNA fragments of Ad-A, B, and C were synthesized by GeneArt Strings DNA Fragments (Thermo Fisher Scientific). The sequences for a fusion protein consisting of circularly permutated GFP (cpGFP; developed in our lab (Nakai et al., 2019)) and each Adhiron were amplified by PCR using PrimeSTAR MAX (TAKARA Bio) and inserted in modified pcDNA3 vector (Zhao et al., 2011), so that these two proteins are connected by a flexible linker (pcDNA3-cpGFP-Ad-A/B/C flex). Then we replaced the flexible linker with 11 different linker sequences shown in Figure S1A by typical restriction enzyme cloning methods (pcDNA3-cpGFP-Ad-A/B/C L1-11).

To make plasmids for mRNA synthesis, POLArIS^{act} sequence and EMTB-mCherry (Addgene plasmid 26742) sequence were amplified by PCR and subcloned into pGEMHE vector using

Gibson Assembly (Gibson et al., 2009) (pGEMHE- POLArIS^{act} and pGEMHE-EMTB-mCherry).

Protein purification and electrophoresis

Coding sequence for cpGFP, Ad-A, or POLArIS^{act} was inserted into the C-terminus of His tag in pRSET B bacterial expression vector (pRSET B-cpGFP, pRSET B-Ad-A or pRSET B-POLArIS^{act}). *E. coli* JM109 (DE3) transformed with these plasmids were precultured in LB medium for 6 h at 37°C, diluted in LB medium at 1:1000, and cultured again for 72 h at 20°C. Cells of *E. coli* were collected by centrifugation and resuspended in TN buffer (50 mM Tris-HCl, 300 mM NaCl, pH 7.4). After cell disruption by sonication, protein was purified using affinity purification with Ni Sepharose 6 Fast Flow (Cytiva). Samples were subjected to SDS-PAGE and stained with CBB staining using Quick-CBB PLUS (FUJIFILM Wako Pure Chemical).

Crystallization and structure determination

Sequence coding POLArIS^{act} T57S mutant was cloned into pET24a bacterial expression vector, so that the N-terminal T7 peptide sequence was removed and the TEV cleavage site was inserted between the C-terminus of Adhiron and the N-terminus of His tag (pET24a-POLArIS^{act} (T57S)). The generated plasmid was transformed into *E.coli* Rosetta (DE3) and the protein was over-expressed overnight at 20°C in LB medium with induction by 0.3 mM IPTG. The cells were collected and were lysed using a sonicator. After centrifugation, the supernatant was applied on a HisTrap HP column (Cytiva) and the target protein was eluted with a linear gradient of imidazole. The His tag was then cleaved by TEV protease and was removed by a HisTrap HP column. The protein was further purified by ion exchange on a HiTrap Q column (Cytiva) and by

size-exclusion chromatography on a HiLoad 16/60 Superdex 75 pg column (Cytiva) in a buffer containing 25 mM Hepes-NaOH (pH 7.5), and 150 mM NaCl.

Crystals were grown at 20°C by the method of sitting drop vapor diffusion with a reservoir solution containing 0.1 M sodium acetate (pH 4.5-5.0) and 6-8% (v/v) PEG 4000. Crystals were cryo-protected with the reservoir solution containing 25% glycerol. Diffraction data were collected at a wavelength of 1.0 Å at SLS beamline X06DA (Villigen). Data were processed with the XDS programs (Kabsch, 2010) and the structure was solved by molecular replacement using the Phaser program (McCoy et al., 2007) from the PHENIX programs (Adams et al., 2010), with the superfolder GFP (PDB ID:4LQT) and the Adhiron (PDB ID:4N6U) as the search models. The structural model was built into the electron density map using COOT (Emsley et al., 2010) and refined using the PHENIX program and Refmac5 from the CCP4 program suite (Winn et al., 2011). The final statistics are summarized in Table S1.

Structural modeling of cpGFP-Adhiron fusion

Modeling of the fusion of proteins was performed on UCSF Chimera. The structure of cpGFP was made by modifying the structure of superfolder GFP (PDB ID:4LQT) and fused with Adhiron (PDB ID:4N6U) with manually constructed linker structures.

Co-sedimentation and pull-down assays

G- and F-actin were prepared from rabbit skeletal muscle actin (AKL99, Cytoskeleton) following the manufacturer's protocol. To depolymerize actin oligomers, actin protein was suspended to 0.4 mg/ml in general actin buffer (5 mM Tris-HCl, 0.2 mM $CaCl_2$, 0.2 mM ATP, 0.5 mM DTT, pH 8.0) and incubated for 1 h on ice. After centrifugation at 4°C for 1 h, at 55,000

rpm using a fixed angle rotor S120AT2 (himac), the supernatant was used as G-actin solution. In F-actin preparation, G-actin suspended in polymerization buffer (5 mM Tris-HCl, 50 mM KCl, 2 mM $MgCl_2$, 0.2 mM $CaCl_2$, 1.2 mM ATP, 0.5 mM DTT, pH 8.0) was incubated at room temperature for 1 h.

Co-sedimentation assay with F-actin were performed as described previously (Lopata et al., 2018). F-actin and POLArIS^{act} were mixed in 50 µl of polymerization buffer with the concentration of 2.5 µM and 1-10 µM, respectively. After incubation at room temperature for 30 min, the mixture was centrifuged at 4°C for 1 h, at 55,000 rpm. SDS sample buffer was added to the supernatant and the pellet and they were boiled at 95°C for 10 min. Ad-A and sfGFP instead of POLArIS^{act} were assayed in the same way as controls. These samples were analyzed by SDS-PAGE using 8% acrylamide gel and stained with CBB staining. Scanned images of gels from three independent sets of experiments were quantified using ImageJ. Based on experimental assumptions that POLArIS^{act} binds to F-actin with 1:1 stoichiometry, which is determined from the result that approximately up to 2.5 µM POLArIS^{act} was co-sedimented with 2.5 µM F-actin, the dissociation constant (K_d) was obtained according to the definition. Each actual value when the concentration of POLArIS^{act} was 1.5-2.5 µM in three sets of assays was substituted into the equation of definition, and the average was calculated as K_d.

In actin pull-down assays, we prepared samples as indicated in Figure S6B in 200 µl of general actin buffer (for samples including G-actin) or polymerization buffer (for samples including F-actin). After incubation at room temperature for 1 h, 20 µl was taken from each sample as “input” fraction and remaining 180 µl was added to 10 µl of washed beads of Ni Sepharose 6 Fast Flow and incubated at room temperature for 1 h with gently mixing. After centrifugation, supernatant was collected as “unbound” fraction. Precipitated beads were washed

with general actin buffer (G-actin samples) or polymerization buffer (F-actin samples), followed by centrifugation again, and supernatant was removed. The beads remained were used as "bound" fraction. Each fraction was mixed with SDS sample buffer, incubated at room temperature for 1 h and then boiled at 95°C for 10 min. These samples were subjected to SDS-PAGE with 8% or 5-11% Bullet PAGE One Precast Gel (nacalai tesque) and stained with CBB staining. Scanned images of gels from three independent sets of experiments were analyzed using ImageJ. *P* values were manually calculated on Microsoft Excel by applying Šidák multiple comparison correction to Student's t-test and difference with $p < 0.01$ was considered significant.

Plasmid introduction into cultured cells

cpGFP-Adhiron expression plasmids constructed as described above were transfected into the HeLa or XTC cells plated on glass-bottom dishes or coverslips using Lipofectamine LTX or 3000 (Thermo Fisher Scientific). The medium was replaced with fresh medium approximately 5 h after transfection. For HeLa M transfection, Polyethylenimine "Max" (24765-1, Polysciences) was used. For live-cell imaging, medium was replaced with DMEM/Ham's F-12 without phenol red (nacalai tesque) or Medium 199 without phenol red (Thermo Fisher Scientific) containing 10% FBS before observation. For LLC-PK1, NEPA21 electroporator (Nepagene) was used to introduce plasmids into cells.

Fixation and staining of cultured cells

To examine the co-localization of cpGFP-Adhiron and F-actin using fluorescent phalloidin, transfected cells were processed for fluorescence staining. The specimens were washed with phosphate-buffered saline (PBS), and then fixed with 4% paraformaldehyde in PBS (pH 7.4).

After permeabilization with 0.1% TritonX-100 for 5 min, the specimens were incubated with 0.5 µg/ml of phalloidin-Atto565 (94072, Merck), 2 µg/ml of Hoechst 33342 (04915-81, nacalai tesque), and 5% skimmed milk in PBS for 1 h at room temperature. Stained cells were washed with PBS and mounted in a mounting solution made of Mowiol 4-88 (ITW Reagents). The intensity profiles of fixed HeLa cells were obtained using imageJ.

In vitro preparation of F-actin and labeling

Purified human platelet actin (APHL99, Cytoskeleton) was polymerized following the manufacturer's protocol and attached to polylysine coated coverslips by incubation with 2 µg/ml actin in actin polymerization solution. Then, specimens were incubated with 10 nM purified recombinant POLArIS^{act} protein or 2-5 nM Alexa Fluor 488 Phalloidin (AF488-phalloidin, A12379, Thermo Fisher Scientific) and 10 mg/ml bovine serum albumin (BSA) in actin polymerization solution for 5 min.

Starfish egg preparation and drug treatment

Asterina pectinifera starfishes were collected on the Pacific coast of Japan and were kept in laboratory aquaria with seawater at 14–15°C. Immature oocytes of *Asterina pectinifera* starfishes were treated with cold calcium-free seawater to remove follicle cells, and then incubated in filtered seawater. Oocytes were microinjected with the mRNA encoding POLArIS^{act} and/or EMTB-mCherry (synthesized *in vitro* from linearized DNA templates using the mMessage mMachine T7 ULTRA Transcription kit (Thermo Fisher Scientific)) on the day before observation and incubated in filtered or artificial seawater (ASW: 423 mM NaCl, 9 mM KCl, 23 mM $MgCl_2$, 25 mM $MgSO_4$, 9 mM $CaCl_2$, 10 mM HEPES, pH 7.4) at 16°C overnight. After

POLArIS^{act} and/or EMTB-mCherry were expressed at the appropriate level, oocytes were treated with 1-Methyladenine (1-MA, KANTO CHEMICAL) to induce maturation.

For observation of early development processes, oocytes were inseminated after germinal vesicle breakdown (GVBD) and incubated at 16°C until microscopic imaging. In pharmacological experiments, embryos were treated with 20 µM Nocodazole (NCZ) (487929, Merck), 10 µM Cytochalasin D (CytoD) (C8273, Merck), 200 µM CK666 (182515, Merck) or 10 µM SMIFH2 (344092, Merck) in ASW at the indicated timing (see Figures legends for details), or perfused with 10 µM SMIFH2 dissolved in ASW by inserting a microneedle into the perivitelline space after fertilization envelope formation. In control experiments, embryos were exposed with ASW containing DMSO. Drugs were dissolved in DMSO to make stock solutions (NCZ, 10 mM; CytoD, 10 mM; CK666, 100 mM; SMIFH2, 50 mM) and the same volume of DMSO as the volume of each stock solution was added to ASW as control.

For observation of fertilization, 1-MA treated eggs were inseminated after GVBD. To perform simultaneous observation of F-actin and DNA, immature eggs were pre-stained with 10 µg/ml Hoechst 33342 for 30 min. Stained eggs were washed with ASW and then treated with 1-MA. Sperms were also stained with 10 µg/ml Hoechst 33342 for 5 min just before insemination. The length of actin bundles (from the point on the cell surface where the bundle appeared to the tip of bundle) in starfish oocytes during fertilization were measured using the Nikon imaging software NIS Elements Advanced Research. Analyses were performed on 8 different eggs.

Immunofluorescence of fixed starfish eggs

Starfish embryos were fixed for 1 h with 3% v/v glyoxal (17226-95, nacalai tesque) fixative solution prepared as described previously (Richter et al., 2018). After fixation, embryos were

washed with PBSw/NaCl (same as PBS except that NaCl concentration was adjusted at 460 mM) and glyoxal was quenched with 100 mM glycine. Embryos were then permeabilized with PBSw/NaCl containing 0.1% TritonX-100, blocked with 0.05% BSA, and sequentially incubated with primary and secondary antibodies dissolved in PBSw/NaCl. To visualize microtubules, YL1/2 rat anti-α-tubulin (MCA77G, Bio-Rad) was used as a primary antibody and goat anti-rat IgG conjugated with Alexa488 (A-11006, Thermo Fisher Scientific) was used as a secondary antibody. To visualize DNA and F-actin, Hoechst 33342 and phalloidin-Atto565 were used, respectively. Stained embryos were placed on a MAS-coated slide glass (Matsunami Glass), mounted with SlowFade Diamond (S36963, Thermo Fisher Scientific), covered with a coverslip, and sealed with nail polish. Observation was carried out within 2 days, as staining with phalloidin-Atto565 was blurred 3 days after glyoxal fixation.

Fluorescence microscopy

Fluorescence microscopic observation of fixed HeLa cells was performed with Nikon Eclipse E600 microscope with dry objective lens (PlanFluor 40x 0.75 N.A., Nikon) or oil immersion objective lens (PlanFluor, 100x 1.30 N.A., Nikon). Images were acquired with the application software ACT-2U (Nikon), and then processed with ImageJ.

Fluorescence microscopic observation of starfish eggs and data acquisition were performed with Nikon Eclipse TiE microscope with dry objective lens (PlanApo 10x 0.45 N.A. and 20x 0.75 N.A., Nikon) and silicone oil immersion objective lenses (UPLSAPO, 30x 1.05 N.A. and 40x 1.25 N.A., Olympus), Nikon C1 CLSM with silicone oil immersion objective lens (UPLSAPO, 40x 1.25 N.A., Olympus), Leica SP8 CLSM (Leica) with oil immersion objective lens (HC PL APO 63x/1.40 Oil CS2, Leica), or Carl Zeiss LSM510 CLSM with water

immersion objective lens (C-Apochromat 40x/1.2 W Corr, Carl Zeiss) in a room kept at 20°C. Images were processed with the Nikon imaging software NIS Elements Advanced Research.

Two-axis Fluorescence Polarization Microscopy

Polarization beam splitting system was assembled at the detection port of Nikon Eclipse TiE (Nakai et al., 2019). In brief, samples were illuminated by the isotropically polarized LED light from SPECTRA light engine (lumencor) and the linear polarization beam splitter splits fluorescence into two orthogonal polarization orientations, 0° (horizontal orientation) and 90° (vertical orientation), and respective images were labeled with pseudo-colors (horizontal polarization, green; vertical polarization, magenta) and merged with the Nikon imaging software NIS Elements Advanced Research. We used dry objective lens (PlanApo 10x 0.45 N.A. and 20x 0.75 N.A., Nikon) and silicone oil immersion objective lenses (UPLSAPO, 30x 1.05 N.A. and 40x 1.25 N.A., Olympus). iXon3 897 EM-CCD camera (Andor Technology) and Zyla 4.2 plus sCMOS (Andor Techonology) were used for detection. Filter cube LF488-C (Semrock) was used for cpGFP-Adhiron fluorescence.

Instantaneous FluoPolScope

Imaging and analysis using Instantaneous FluoPolScope were performed as reported previously (Mehta et al., 2016; Nakai et al., 2019). The excitation illumination achieves isotropic polarization at the specimen plane. Fluorescence images were collected with a high NA objective lens (PlanApo TIRF 100x 1.49NA oil, Nikon). In the collimated space, linear polarization beam splitters separate the fluorescence into four images and analyze their linear polarization along 0˚, 45˚, 90˚ and 135˚ orientations. Based on the intensity imbalance of polarized fluorescence along

four orientations, polarization factor and the orientation of its maximum polarization of the objects are computed.

Calculation of the polarization value (PV)

For quantification of fluorescence anisotropy of cpGFP-Adhiron constructs, transfected HeLa M cells were arrested in mitosis using thymidine-nocodazole method. HeLa M cells were treated with 2 mM thymidine for 20 h, and released for overnight in the presence of 100 ng/mL nocodazole. We defined Polarization Value (PV) as

$$\mathrm{PV} = \frac{I(\mathrm{Ver})^{\mathrm{norm}} - I(\mathrm{Hor})^{\mathrm{norm}}}{I(\mathrm{Ver})^{\mathrm{norm}} + I(\mathrm{Hor})^{\mathrm{norm}}},$$

where $I(\mathrm{Ver})^{\mathrm{norm}}$ = [cortex ROI intensity (Ver) – background (Ver)], $I(\mathrm{Hor})^{\mathrm{norm}}$ = [cortex ROI intensity (Hor) – background (Hor)]·CF, and CF = total intensity (Ver) / total intensity (Hor). The mean intensity of a small rectangle ROI enclosing vertical cortex in the cross section of a mitotic cell was measured both in vertical polarization and horizontal polarization images to calculate cortex ROI intensity (Ver) and cortex ROI intensity (Hor), respectively. The mean intensity of a square ROI outside of the cell was measured both in the same vertical polarization and horizontal polarization images to calculate background (Ver) and background (Hor), respectively. CF (correction factor) was calculated by the ratio of the mean ROI intensities between vertical and horizontal polarization images that contain a whole cell, using images of cells expressing cpGFP-Ad-A flex. Examples of ROI settings are shown in Figure S2A. Positive PV values indicate the polarization is parallel to the axis of actin filaments, and negative PV values indicate the perpendicular polarization. n = 10 for each calculation. *P* values against cpGFP-Ad-A (flex) were manually calculated on Microsoft Excel by applying Šidák multiple comparison correction to Student's t-test. Difference with $p < 0.01$ was considered significant.

Analysis of the cross pattern of FLARE

The presence of the green (horizontal)/magenta (vertical) cross patterns and their centers were deduced using the strategy as detailed below. Suppose a polar coordinate system (r, φ) is set over the radial F-actin array, and the transition dipole moments (TDMs) of the fluorophores of POLArIS^{act} are aligned on each F-actin filament. When the fluorophores are excited by vertical polarization (parallel to line φ = 0), the fluorescence efficiency of each fluorophore varies with the angle between the polarized excitation and the TDMs. Thus, the distribution of observed fluorescence intensity $\mathrm{Fl}_{\mathrm{vertical}}$ can be modeled as:

$$\mathrm{Fl}_{\mathrm{vertical}}(r,\varphi) = f_{\mathrm{FLARE}}(r)cos^2(\varphi) + f_{\text{non-radial}}(r,\varphi) + \text{noise},$$

where $f_{\mathrm{FLARE}}(r)$ is the radial profile of the fluorescent component that is aligned on radial F-actin array, and $f_{\text{non-radial}}(r,\varphi)$ is the fluorescent component that is not radially aligned. The distribution of fluorescence intensity $\mathrm{Fl}_{\mathrm{horizontal}}$ to be observed with horizontal excitation will be:

$$\mathrm{Fl}_{\mathrm{horizontal}}(r,\varphi) = f_{\mathrm{FLARE}}(r)cos^2\left(\varphi - \frac{\pi}{2}\right) + f_{\text{non-radial}}(r,\varphi) + \text{noise}$$

$$= f_{\mathrm{FLARE}}(r)sin^2(\varphi) + f_{\text{non-radial}}(r,\varphi) + \text{noise}.$$

Then the polarization differential image intensity $\mathrm{Fl}_{\mathrm{diff}}$ of these two will be modeled as:

$$\mathrm{Fl}_{\mathrm{diff}}(r,\varphi) = \mathrm{Fl}_{\mathrm{vertical}}(r,\varphi) - \mathrm{Fl}_{\mathrm{horizontal}}(r,\varphi)$$

$$= f_{\mathrm{FLARE}}(r)cos(2\varphi) + \text{noise}.$$

Thus, fluorophores aligned on a radial F-actin array show a fluorescence intensity pattern that varies with cos(2φ) when measured along the circle of fixed radius around the center of the array in the differential image. Conversely, if this characteristic pattern is found on the polarization differential image, it suggests the possible presence of a radial F-actin array there.

Based on this, we used the following algorithm to search for the presence of cross patterns. First, we created a kernel image with this characteristic intensity pattern of cos(2φ):

$$\text{pixel value at} \quad (x, y) = (x_{\text{center}} - r sin\varphi, y_{\text{center}} - r cos\varphi) \quad \text{is}$$

$$\begin{cases} \dfrac{cos(2\varphi)}{r_{\max} - r_{\min} + 1} & \text{if} \quad r_{\min} - \dfrac{1}{2} \leq r < r_{\max} + \dfrac{1}{2} \\ 0 & \text{otherwise,} \end{cases},$$

where $(x_{\text{center}}, y_{\text{center}})$ is the center of the kernel image, and $r_{\min}$ and $r_{\max}$ specifies the size of the concentric area to look for. Then, we convolved the polarization differential images with this cos(2φ) kernel image. Each pixel value of the convolved result is related to the likelihood of the presence of the cos(2φ) pattern with the center at that pixel. We inspected several points with local maximal values as candidates and determined the center of radial F-actin arrays.

The radial extent of the F-actin array was not readily discernable because it was blurred in the noisy background. So, to help visualize the radial profile, we rotated the polarization differential image around the center of the array and calculated the autocorrelation at each radius G_{rot}:

$$G_{\text{rot}}(r, \theta) = \frac{\int_0^{2\pi} \text{Fl}_{\text{diff}}(r, \varphi) \text{Fl}_{\text{diff}}(r, \varphi + \theta) d\varphi}{\int_0^{2\pi} [\text{Fl}_{\text{diff}}(r, \varphi)]^2 d\varphi}, 0 \leq \theta \leq 2\pi$$

The rotational autocorrelation above was normalized to have a value of 1 at $\theta = 0$ or $\theta = 2\pi$. Bicubic interpolation was used for subpixel sampling when calculating the autocorrelation of pixel values from the differential image. The rotational autocorrelation of the radial FLARE component becomes:

$$G_{\text{rot,FLARE}}(r, \theta) = \frac{\int_0^{2\pi} f_{\text{FLARE}}(r) cos(2\varphi) f_{\text{FLARE}}(r) cos(2(\varphi + \theta)) d\varphi}{\int_0^{2\pi} [f_{\text{FLARE}}(r) cos(2\varphi)]^2 d\varphi}$$

$$= \frac{[f_{\text{FLARE}}(r)]^2 \int_0^{2\pi} cos(2\varphi) cos(2(\varphi + \theta)) d\varphi}{[f_{\text{FLARE}}(r)]^2 \int_0^{2\pi} [cos(2\varphi)]^2 d\varphi} = cos(2\theta)$$

This curve takes a local maximum at $\theta = \pi$ and local minima at $\theta = \frac{\pi}{2}$ and $\theta = \frac{3\pi}{2}$. In contrast, the autocorrelation of the noise component is expected to have a sagging profile with minimum at $\theta = \pi$. The shape of $G_{\mathrm{rot}}(r, \theta)$ surface calculated from actual differential images will depend on the relative intensity of the radial FLARE component and the noise, but the presence of a peak at $\theta = \pi$ in the rotational autocorrelation will be a good indicator of the presence of the cross pattern at radius r. The algorithms described above were packaged as an ImageJ plugin and deposition of the plugin at GitLab is in progress.

Obtained 2D-plots of the rotational autocorrelation for each radius were converted to 3D-plots using ImageJ 'surface plot' function.

Supplemental Information

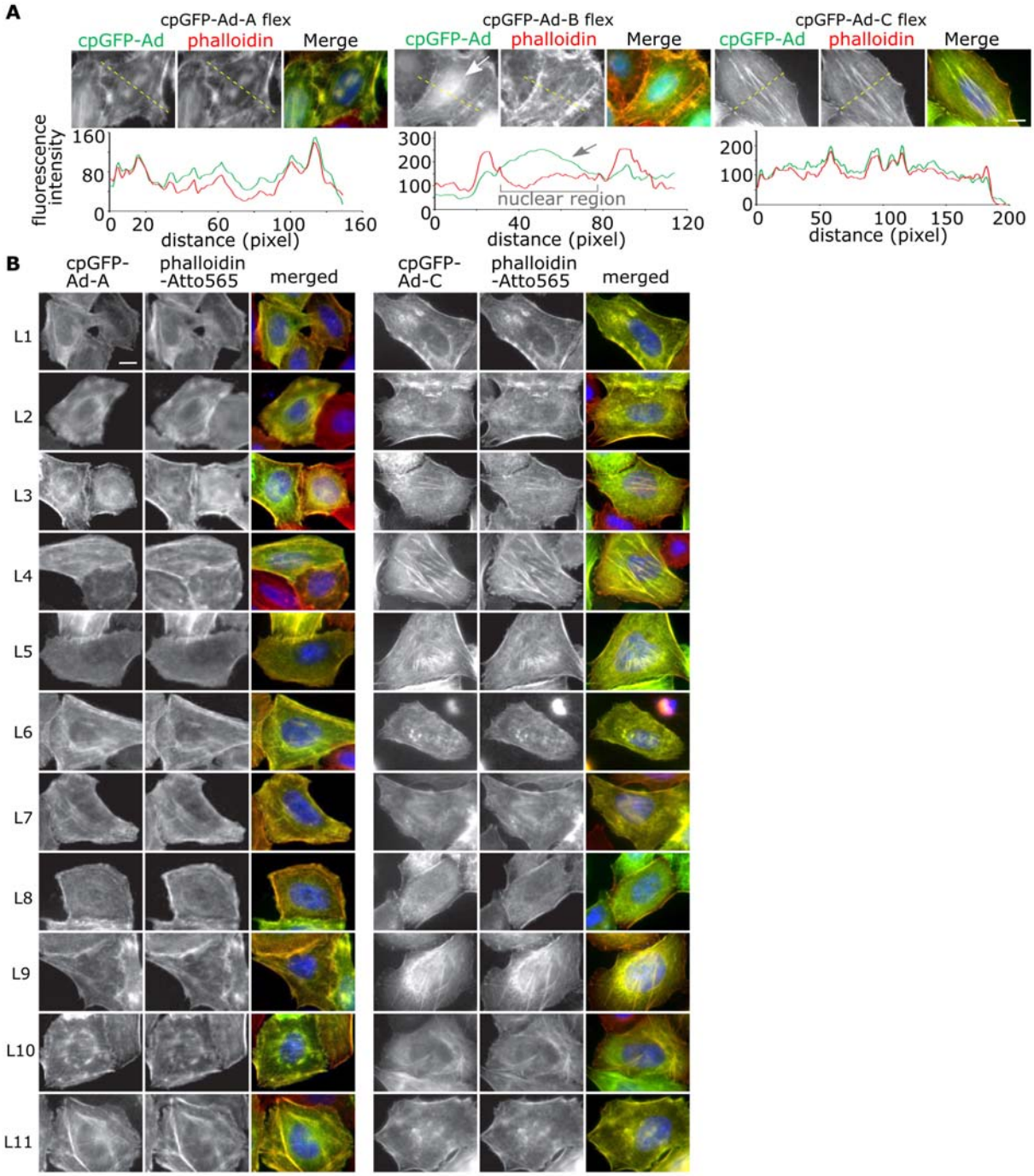

Figure S1. Detailed information of cpGFP-Adhiron constructs and their localization analysis.

(A) Top row: Representative fluorescence microscopy images of fixed HeLa cells expressing cpGFP-Ad-A/B/C flex (left panels) with phalloidin-Atto565 (middle panels) staining. Merged

images of cpGFP-Adhiron (green), phlloidin-Atto565 (red) and DNA stained with Hoechst (blue) are also shown in right panels. Bottom row: Intensity profiles for cpGFP-Ad-A/B/C and phalloidin-Atto565 channels along the dashed yellow lines marked on the images in top panels. Arrows show the high background in nuclear region of cpGFP-Ad-B flex fluorescence. Scale bar: 10 µm.

(B) Co-localization analysis of cpGFP-Adhirons with actin filaments stained with phalloidin. Representative fluorescence microscopy images of fixed HeLa cells expressing cpGFP-Ad-A/C L1-L11 (left columns) with phalloidin-Atto565 (middle columns) staining are shown. Merged images of cpGFP-Adhiron (green), phlloidin-Atto565 (red) and DNA stained with Hoechst (blue) are shown in right columns. Scale bar: 10 µm.

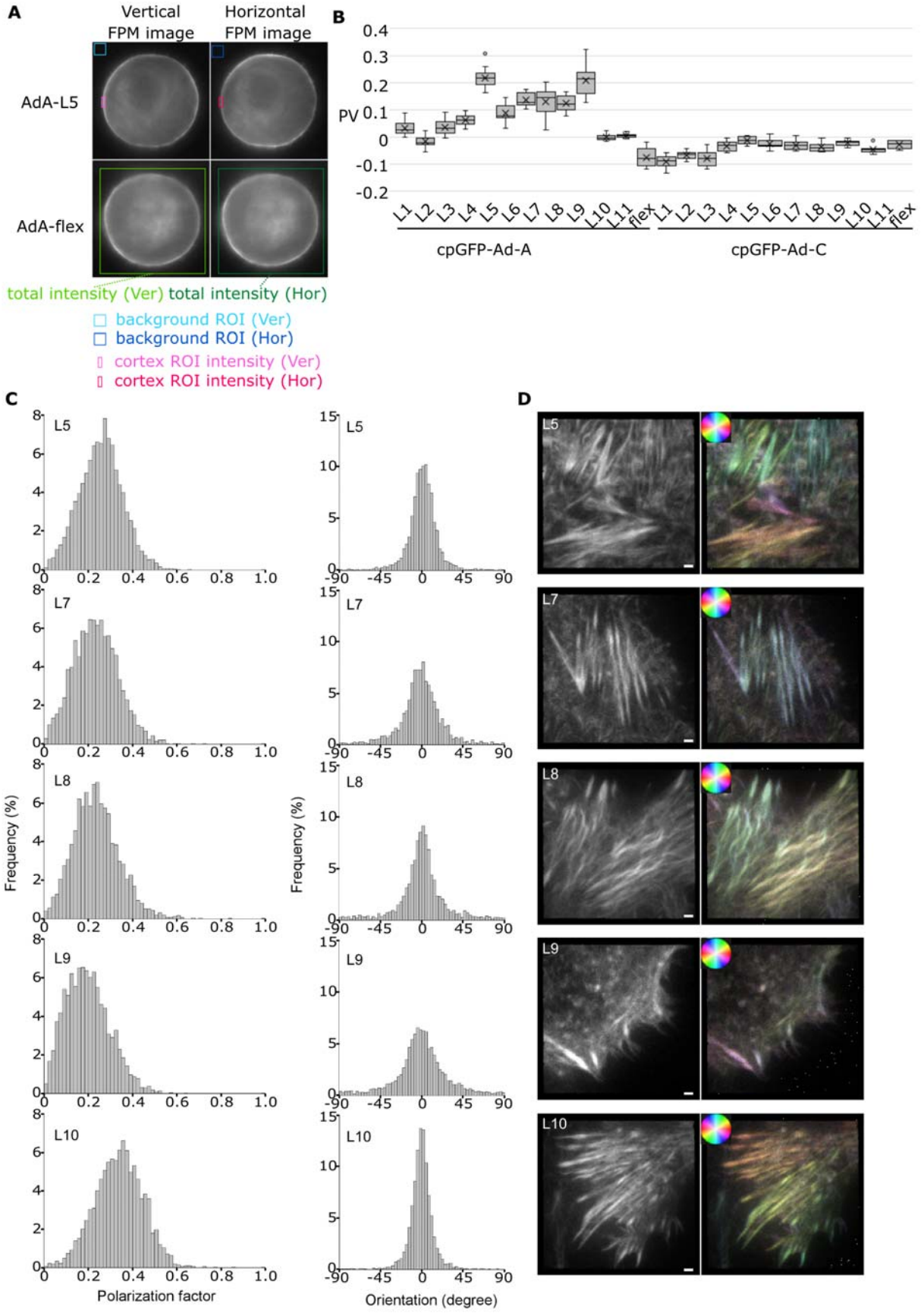
A
Vertical FPM image
Horizontal FPM image
AdA-L5
AdA-flex
total intensity (Ver)
total intensity (Hor)
background ROI (Ver)
background ROI (Hor)
cortex ROI intensity (Ver)
cortex ROI intensity (Hor)
B
PV
L1 L2 L3 L4 L5 L6 L7 L8 L9 L10 L11 flex
cpGFP-Ad-A
cpGFP-Ad-C
C
Frequency (%)
Polarization factor
Orientation (degree)
D

Figure S2. Screening of cpGFP-Adhiron constructs by quantifying polarization of fluorescence in living cells.

(A) Examples of ROI settings in two-axis FPM images for calculation of Polarization Value (PV) of cpGFP-Ad-A L5 are shown. See STAR Methods for details of PV calculation.

(B) PVs for all cpGFP-Ad constructs are shown by boxplots with cross marks indicating averages (n=10).

(C) Instantaneous FluoPolScope analysis of five cpGFP-Ad-A constructs (L5, 7, 8, 9 and 10) expressed in LLC-PK1 cells, and the results of polarization factor (left) and polarization orientation (right) are shown in histograms. The ordinates of histograms are the frequencies of detected particles. Orientation at 0° indicates the polarization orientation of the particle is parallel to actin filaments, and orientation at -90° or 90° indicates the polarization orientation of the particle is perpendicular to actin filaments.

(D) Representative images of instantaneous FluoPolScope analysis. Left panels show the ensemble fluorescence intensity of four polarization orientations, and right panels show the orientation of ensemble polarization by pseudo-color. The hue color circles in right panels show the relationship between pseudo-color and orientation of ensemble polarization. Scale bar: 1 μm.

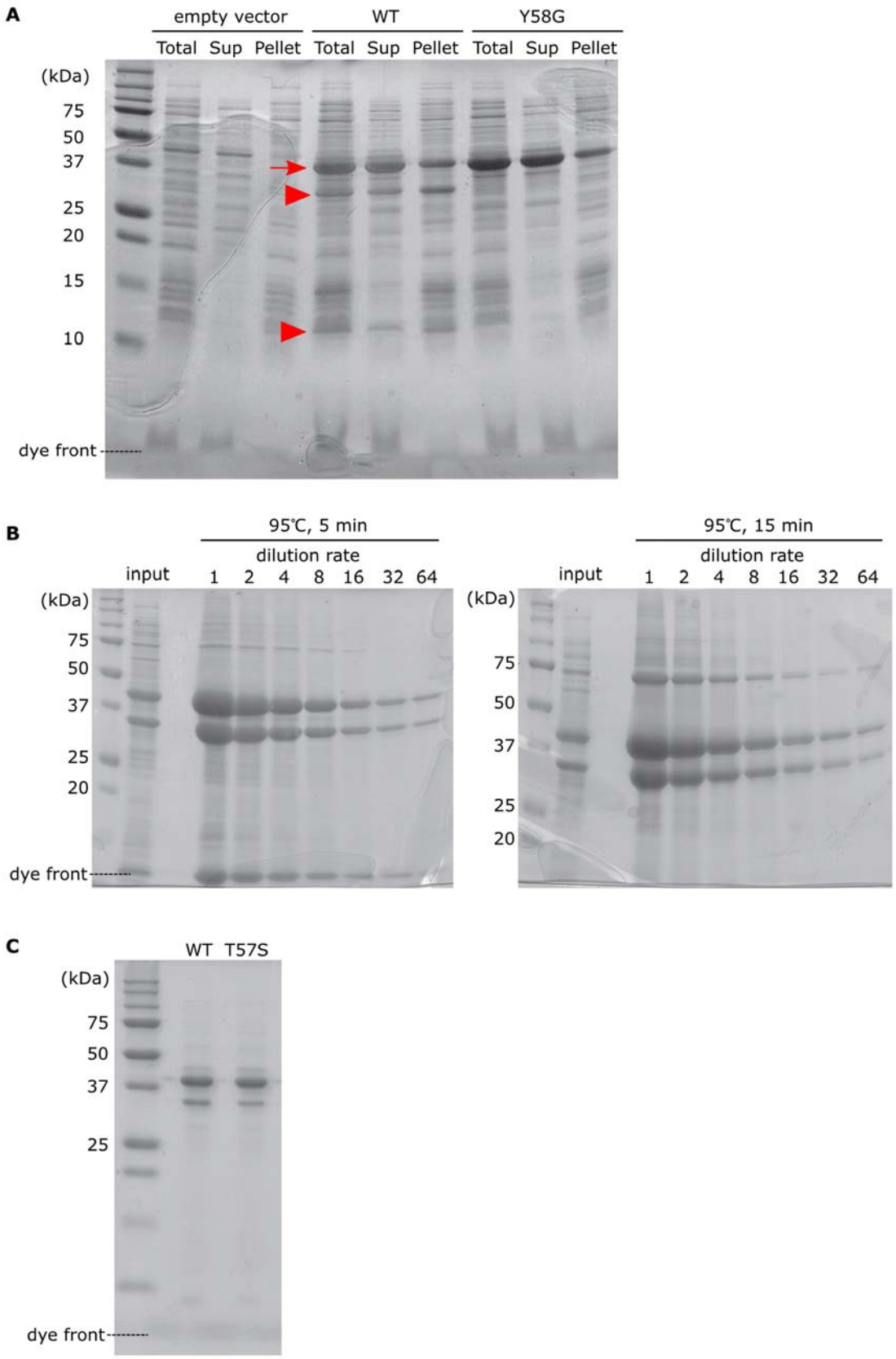
A
empty vector
WT
Y58G
Total Sup Pellet Total Sup Pellet Total Sup Pellet
(kDa)
75
50
37
25
20
15
10
dye front
B
95℃, 5 min
dilution rate
input 1 2 4 8 16 32 64
(kDa)
75
50
37
25
20
dye front
95℃, 15 min
dilution rate
input 1 2 4 8 16 32 64
(kDa)
75
50
37
25
20
C
WT T57S
(kDa)
75
50
37
25
dye front

Figure S3. Selection of POLArIS^{act} mutants suitable for structure determination.

(A) CBB-stained SDS-PAGE gel of whole protein (Total), supernatant (Sup) and pellet of *E. coli* JM109 (DE3) bacterial cells expressing POLArIS^{act} or its Y58G variant. POLArIS^{act} protein (WT) unexpectedly produced extra bands at 32 kDa and 11 kDa (arrowheads) in addition to the expected band of 40 kDa (arrow). Extra bands disappeared when the Y58G mutant, which is expected to prevent cpGFP from forming the chromophore, was used, indicating that extra bands were produced due to "backbone fragmentation," during chromophore formation or maturation.

(B) CBB-stained SDS-PAGE gels of purified POLArIS^{act}. Proteins were purified from POLArIS^{act}-expressing bacterial cells and prepared samples were heated at 95°C for 5 min (left) or 15 min (right) and loaded onto gels with sequential dilutions. The production of extra bands shown in (A) is unlikely to be caused by the incompletion of protein denaturation, as the intensities of extra bands were not affected by the difference of the length of the heating.

(C) CBB-stained SDS-PAGE gel of purified wild-type POLArIS^{act} (WT) and its mutant (T57S) proteins. T57S mutant of POLArIS^{act} was comparatively resistant to "backbone fragmentation" and used for the crystal structure analysis.

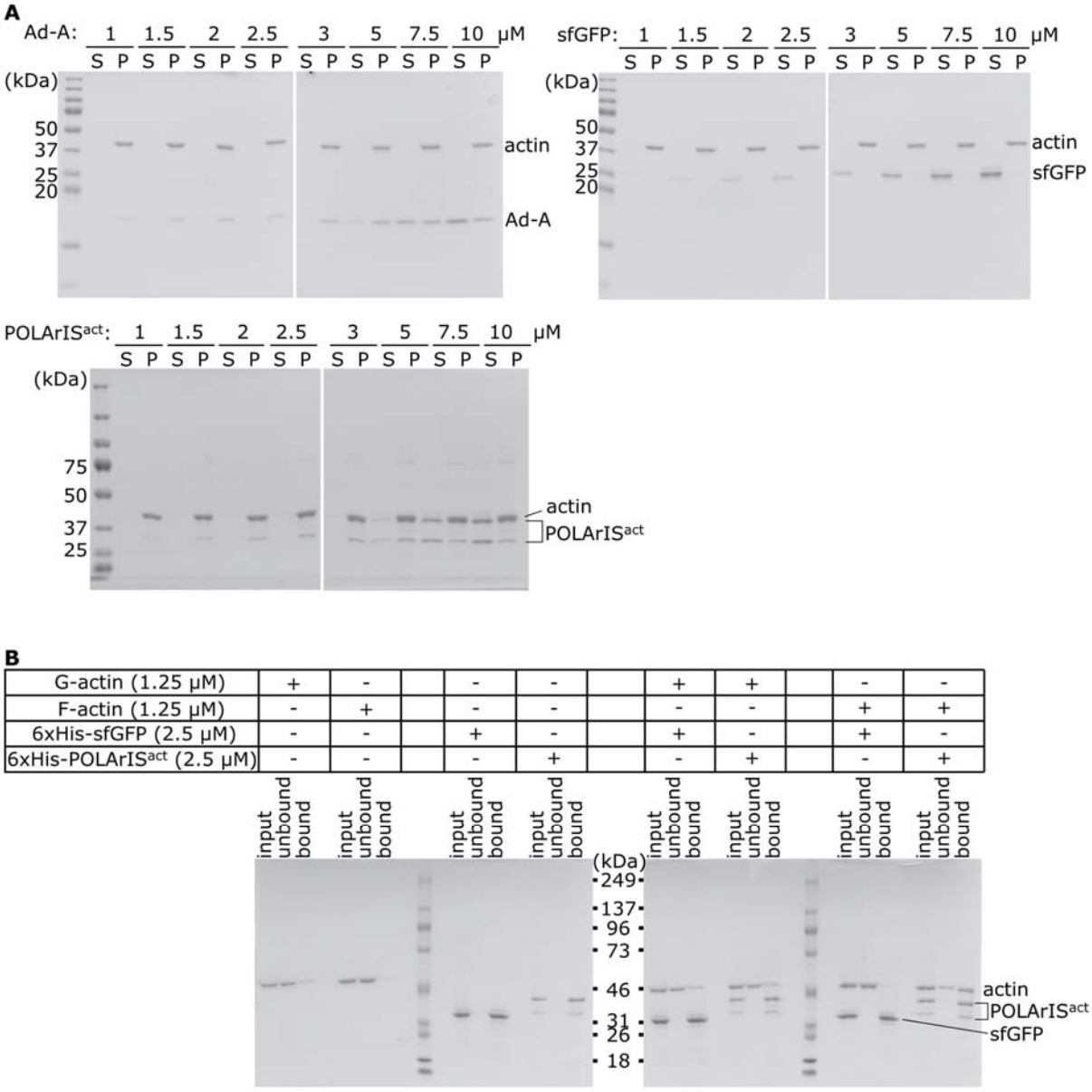

Figure S4. Co-sedimentation and pull-down assays to analyze interaction between POLArISact and F-actin.

(A) CBB staining of typical SDS-PAGE gels of co-sedimentation assay in which 2.5 μM F-actin were mixed with increasing concentrations of Ad-A (top left), sfGFP (top right) or POLArIS^{act}

(bottom). Lanes show supernatant (S) and pellet (P) of each mixture with different concentrations of proteins.

(B) CBB staining of typical SDS-PAGE gels of actin pull-down assay. Components of each reaction are shown in the list. Bound fraction was twice as concentrated as input and unbound fractions.

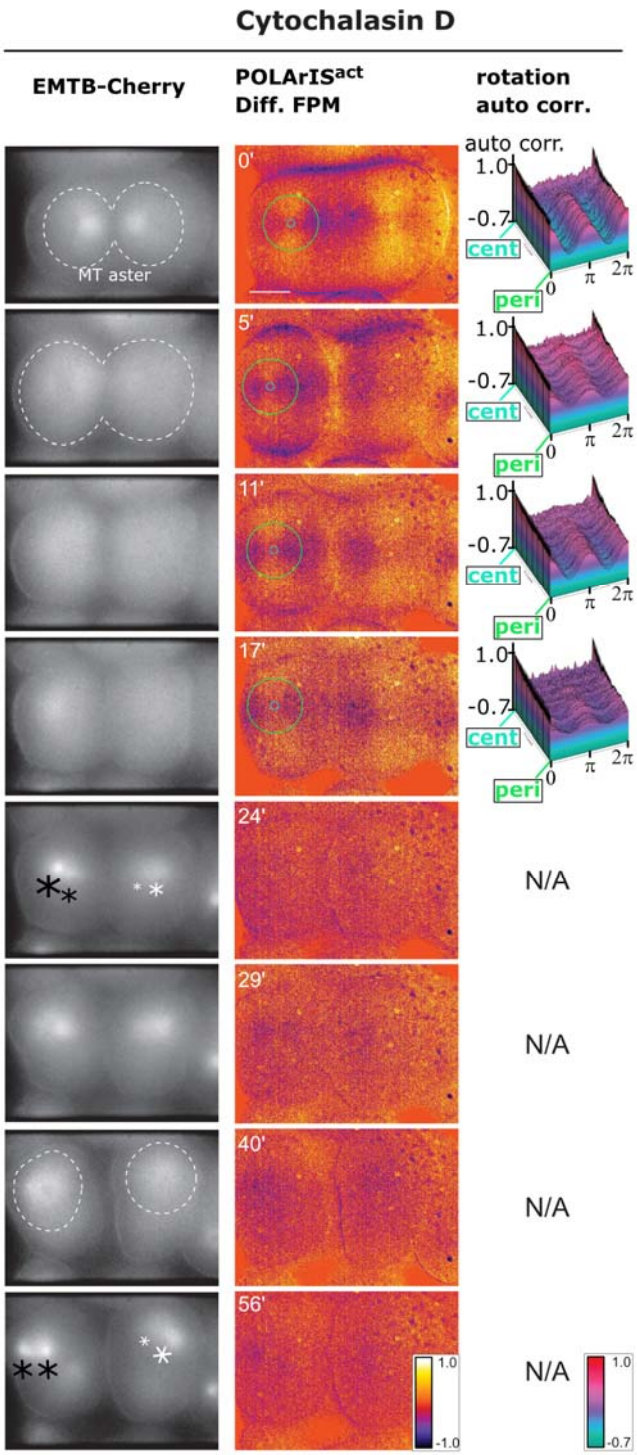
Cytochalasin D
EMTB-Cherry
POLArIS act
Diff. FPM
rotation
auto corr.
MT aster
0'
5'
11'
17'
24'
29'
40'
56'
auto corr.
1.0
-0.7
cent
peri
0
π
2π
N/A
1.0
-1.0
1.0
-0.7

Figure S5. Microtubule aster dynamics does not depend on FLARE.

Time lapse two-axis FPM observation of a Cytochalasin D-treated embryo expressing POLArIS^{act} and EMTB-mCherry in the fourth cleavage. Left column shows vertical polarization images of EMTB-mCherry, middle column shows differential FPM images of POLArIS^{act} with circles of min/max diameters used in autocorrelation analyses, and right column shows 3D-plots of autocorrelation analyses of FLARE. Asterisks indicate centrosomes, dashed lines indicate contours of microtubule asters. Scale bar: 50 µm.

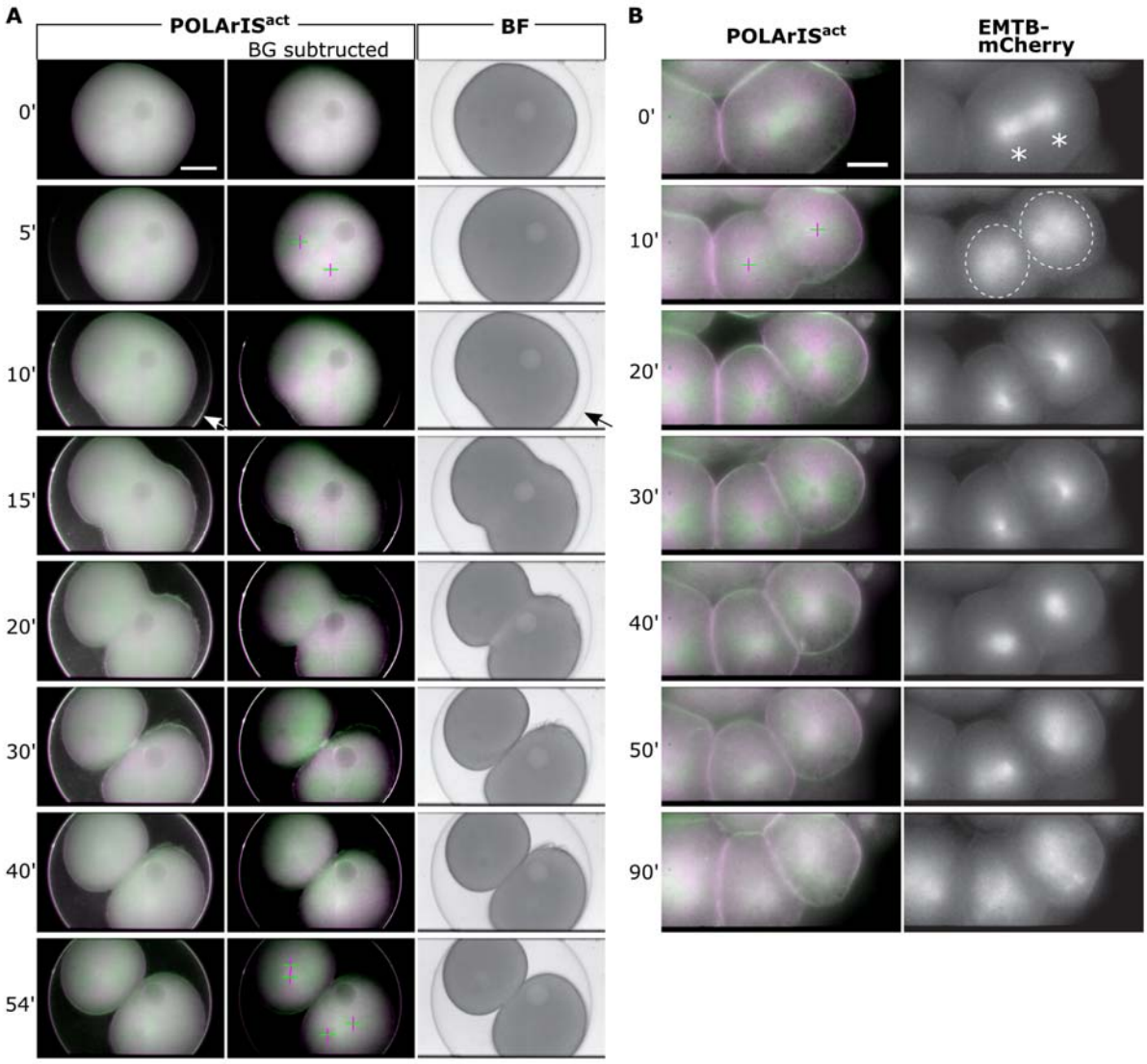

Figure S6. Time lapse observations of SMIFH2 treated starfish embryos.

(A) A starfish embryo expressing POLArIS^{act} was treated with SMIFH2 before the first cleavage (time 0). Images by two-axis FPM (left and middle columns) and their bright field view (right column). In panels of middle column, background signal was subtracted for the better presentation of green/magenta cross patterns. Arrows indicate the fertilization envelope and cross marks indicate the centers of the cross patterns of FLARE structures. Accumulation of the drug on fertilization envelope was evident 10 min after the drug addition. Scale bar: 50 µm.

(B) A starfish embryo expressing POLArIS^{act} and EMTB-mCherry was treated with SMIFH2 with microinjection under the elevated fertilization envelope and observed with two-axis FPM. The drug was added just after microtubule asters started to extend during the fourth cleavage (time 0). Left column shows green/magenta FPM images of POLArIS^{act} and right column shows vertical polarization images of EMTB-mCherry. Cross marks indicate the centers of the green/magenta cross patterns. Asterisks indicate centrosomes, dashed lines indicate contours of microtubule asters. Scale bar: 25 µm.

Data collection and processing	
Beamline	X06DA, SLS
Space group	$I\,2_1\,2_1\,2_1$
Unit-cell parameter	
a, b, c (Å)	78.1, 113.6, 132.7
α, β, γ (˚)	90.0, 90.0, 90.0
Wavelength (Å)	1.000
Resolution range (Å)	50.0–2.50 (2.64–2.50)
Redundancy	7.1 (7.1)
Completeness (%) [a]	99.9 (99.8)
R_{sym} [b] (%) [a]	1.62 (9.6)
I/σ (I) [a]	13.3 (1.0)
No. monomers/asymmetric unit	1
Model refinement	
No. of reflections	20785
No. of protein atoms	2528
No. of water molecules	81
R_{work}/R_{free} (%)	21.4/23.8
r.m.s.d. for bond length (Å)	0.003
r.m.s.d. for bond angles (˚)	0.633
Residues in the Ramachandran plot	
Favored region (%)	95.7
Allowed regions (%)	2.6
PDB ID	XXXX

[a] Statistics for the highest resolution shell are given in parentheses.

[b] $R_{sym} = \sum_{hkl} \sum_i |I_i(hkl) - \langle I(hkl) \rangle| / \sum_{hkl} \sum_i I_i(hkl)$.

Table S1.

Movie S1.

A representative movie of the single particle observation of POLArIS^{act} with Instantaneous FluoPolScope in a lamellipodium of a living XTC cell expressing POLArIS^{act}. Left panels show the ensemble fluorescence intensity of instantaneous FluoPolScope and right panels show the polarization factor and the orientations of polarized fluorescence (indicated by yellow lines, yellow scale bar shows the maximum polarization factor) of detected POLArIS^{act} particles (yellow circles). x312 actual speed.

Movie S2.

Time lapse of two-axis FPM (green/magenta) of starfish oocytes expressing POLArIS^{act} during breakdown of the GV and formation of the F-actin meshwork, related to Figure 3A. Time 0 is just before the breakdown, about 27 min after 1-MA addition. Arrow indicates GV, and arrowheads indicate actin filaments with clear polarization in the meshwork (green: horizontal, magenta: vertical). x236 actual speed.

Movie S3.

Time lapse of starfish oocytes expressing POLArIS^{act} during the polar body extrusion with two-axis green/magenta FPM (left) and bright field view (right), related to Figure 3B. The positions of the polar body extrusion and the accumulation of contractile ring-like F-actin are shown by arrowhead and arrow, respectively. x312 actual speed.

Movie S4.

Fluorescence microscopy time lapse of the fertilization of starfish oocyte expressing POLArIS^{act} with Hoechst staining, related to Figure 3D. Top shows the entire egg, and bottom magnifies the area where the actin bundle, DNA of the egg (arrowheads) and sperm (arrows) were observed. Left: POLArIS^{act}, middle: Hoechst, right: merged (POLArIS^{act}: green, Hoechst: magenta). x240 actual speed.

Movie S5.

Time lapse during the first cleavage of a starfish egg expressing POLArIS^{act} with two-axis FPM (green/magenta), related to Figure 4A. In the first half, cross marks indicate the centers of the green/magenta cross patterns. These illustrations are omitted from the second half. x505 actual speed.

Movie S6.

Overnight time lapse two-axis FPM (green/magenta) after the fourth cleavage of a starfish embryo expressing POLArIS^{act}, related to Figure 4B. Cross marks indicate the centers of the green/magenta cross patterns. x612 actual speed.

Movie S7.

Time lapse green/magenta FPM movie of the first cleavage of a starfish egg expressing POLArIS^{act} and EMTB-mCherry, related to Figure 5C. For EMTB-mCherry, only vertical polarization images were shown. In the first half, cross marks indicate the centers of FLARE, and asterisks and dashed line indicate centrosomes and contours of microtubule asters, respectively. These illustrations are omitted from the second half. x900 actual speed.

References:

Adams, P.D., Afonine, P. V, Bunkóczi, G., Chen, V.B., Davis, I.W., Echols, N., Headd, J.J., Hung, L.W., Kapral, G.J., Grosse-Kunstleve, R.W., et al. (2010). PHENIX: A comprehensive Python-based system for macromolecular structure solution. Acta Crystallogr. Sect. D Biol. Crystallogr. *66*, 213–221.

Amann, K.J., and Pollard, T.D. (2001). The Arp2/3 complex nucleates actin filament branches from the sides of pre-existing filaments. Nat. Cell Biol. *3*, 306–310.

Arai, R., Ueda, H., Kitayama, A., Kamiya, N., and Nagamune, T. (2001). Design of the linkers which effectively separate domains of a bifunctional fusion protein. Protein Eng. *14*, 529–532.

Barondeau, D.P., Kassmann, C.J., Tainer, J.A., and Getzoff, E.D. (2006). Understanding GFP posttranslational chemistry: Structures of designed variants that achieve backbone fragmentation, hydrolysis, and decarboxylation. J. Am. Chem. Soc. *128*, 4685–4693.

Bedford, R., Tiede, C., Hughes, R., Curd, A., McPherson, M.J., Peckham, M., and Tomlinson, D.C. (2017). Alternative reagents to antibodies in imaging applications. Biophys. Rev. *9*, 299–308.

Brejc, K., Sixma, T.K., Kitts, P.A., Kain, S.R., Tsien, R.Y., Ormö, M., and Remington, S.J. (1997). Structural basis for dual excitation and photoisomerization of the Aequorea victoria green fluorescent protein. Proc. Natl. Acad. Sci. U. S. A. *94*, 2306–2311.

DeMay, B.S., Bai, X., Howard, L., Occhipinti, P., Meseroll, R.A., Spiliotis, E.T., Oldenbourg, R., and Gladfelter, A.S. (2011). Septin filaments exhibit a dynamic, paired organization that is conserved from yeast to mammals. J. Cell Biol. *193*, 1065–1081.

Emsley, P., Lohkamp, B., Scott, W.G., and Cowtan, K. (2010). Features and development of Coot. Acta Crystallogr. Sect. D Biol. Crystallogr. *66*, 486–501.

Farina, F., Gaillard, J., Guérin, C., Couté, Y., Sillibourne, J., Blanchoin, L., and Théry, M. (2016). The centrosome is an actin-organizing centre. Nat. Cell Biol. *18*, 65–75.

Farina, F., Ramkumar, N., Brown, L., Samander□Eweis, D., Anstatt, J., Waring, T., Bithell, J., Scita, G., Thery, M., Blanchoin, L., et al. (2019). Local actin nucleation tunes centrosomal microtubule nucleation during passage through mitosis. EMBO J. e99843.

Field, C.M., Pelletier, J.F., and Mitchison, T.J. (2019). Disassembly of actin and keratin networks by Aurora B kinase at the midplane of cleaving Xenopus laevis eggs. Curr. Biol. *29*, 1999-2008.e4.

Gibson, D.G., Young, L., Chuang, R.-Y., Venter, J.C., Hutchison, C.A., and Smith, H.O. (2009). Enzymatic assembly of DNA molecules up to several hundred kilobases. Nat. Methods *6*, 343–345.

Hamaguchi, Y., and Mabuchi, I. (1982). Effects of phalloidin microinjection and localization of fluorescein□labeled phalloidin in living sand dollar eggs. Cell Motil. *2*, 103–113.

Hamaguchi, Y., Numata, T., and K. Satoh, S. (2007). Quantitative analysis of cortical actin filaments during polar body formation in starfish oocytes. Cell Struct. Funct. *32*, 29–40.

Hughes, D.J., Tiede, C., Penswick, N., Tang, A.A.S., Trinh, C.H., Mandal, U., Zajac, K.Z., Gaule, T., Howell, G., Edwards, T.A., et al. (2017). Generation of specific inhibitors of SUMO-1- and SUMO-2/3-mediated protein-protein interactions using Affimer (Adhiron) technology. Sci. Signal. *10*, eaaj2005.

Inoue, D., Obino, D., Pineau, J., Farina, F., Gaillard, J., Guerin, C., Blanchoin, L., Lennon□Duménil, A., and Théry, M. (2019). Actin filaments regulate microtubule growth at the centrosome. EMBO J. e99630.

Inoué, S. (1953). Polarization optical studies of the mitotic spindle. Chromosoma *5*, 487–500.

Inoué, S. (1981). Cell division and the mitotic spindle. J. Cell Biol. *91*, 131–147.

Inoué, S., Shimomura, O., Goda, M., Shribak, M., and Tran, P.T. (2002). Fluorescence polarization of green fluorescence protein. Proc. Natl. Acad. Sci. U. S. A. *99*, 4272–4277.

Kabsch, W. (2010). XDS. Acta Crystallogr. Sect. D *66*, 125–132.

Kampmann, M., Atkinson, C.E., Mattheyses, A.L., and Simon, S.M. (2011). Mapping the orientation of nuclear pore proteins in living cells with polarized fluorescence microscopy. Nat. Struct. Mol. Biol. *18*, 643–649.

Lamason, R.L., and Welch, M.D. (2017). Actin-based motility and cell-to-cell spread of bacterial pathogens. Curr. Opin. Microbiol. *35*, 48–57.

Lénárt, P., Bacher, C.P., Daigle, N., Hand, A.R., Eils, R., Terasaki, M., and Ellenberg, J. (2005). A contractile nuclear actin network drives chromosome congression in oocytes. Nature *436*, 812–818.

Lopata, A., Tiede, C., Tomlinson, D.C., Sellers, J.R., Knight, P.J., and Peckham, M. (2016). Artificial actin-binding proteins with novel multifunctional properties. Biophisical Soc. 60th Annu. Meet. L3598-Pos, Los Angeles, California, 02 Mar.

Lopata, A., Hughes, R., Tiede, C., Heissler, S.M., Sellers, J.R., Knight, P.J., Tomlinson, D., and Peckham, M. (2018). Affimer proteins for F-actin: Novel affinity reagents that label F-actin in live and fixed cells. Sci. Rep. *8*, 6572.

McCoy, A.J., Grosse-Kunstleve, R.W., Adams, P.D., Winn, M.D., Storoni, L.C., and Read, R.J. (2007). Phaser crystallographic software. J. Appl. Crystallogr. *40*, 658–674.

Mehta, S.B., McQuilken, M., La Riviere, P.J., Occhipinti, P., Verma, A., Oldenbourg, R., Gladfelter, A.S., and Tani, T. (2016). Dissection of molecular assembly dynamics by tracking

orientation and position of single molecules in live cells. Proc. Natl. Acad. Sci. *113*, E6352–E6361.

Miller, A.L., and Bement, W.M. (2009). Regulation of cytokinesis by Rho GTPase flux. Nat. Cell Biol. *11*, 71–77.

Mori, M., Monnier, N., Daigle, N., Bathe, M., Ellenberg, J., and Lénárt, P. (2011). Intracellular transport by an anchored homogeneously contracting F-actin meshwork. Curr. Biol. *21*, 606–611.

Mori, M., Somogyi, K., Kondo, H., Monnier, N., Falk, H.J., MacHado, P., Bathe, M., Nédélec, F., and Lénárt, P. (2014). An Arp2/3 nucleated F-actin shell fragments nuclear membranes at nuclear envelope breakdown in starfish oocytes. Curr. Biol. *24*, 1421–1428.

Nakai, N., Sato, K., Tani, T., Saito, K., Sato, F., and Terada, S. (2019). Genetically encoded orientation probes for F-actin for fluorescence polarization microscopy. Microscopy *68*, 359–368.

Nishizaka, T., Oiwa, K., Noji, H., Kimura, S., Muneyuki, E., Yoshida, M., and Kinosita, K. (2004). Chemomechanical coupling in F1-ATPase revealed by simultaneous observation of nucleotide kinetics and rotation. Nat. Struct. Mol. Biol. *11*, 142–148.

Nolen, B.J., Tomasevic, N., Russell, A., Pierce, D.W., Jia, Z., McCormick, C.D., Hartman, J., Sakowicz, R., and Pollard, T.D. (2009). Characterization of two classes of small molecule inhibitors of Arp2/3 complex. Nature *460*, 1031–1034.

Pettersen, E.F., Goddard, T.D., Huang, C.C., Couch, G.S., Greenblatt, D.M., Meng, E.C., and Ferrin, T.E. (2004). UCSF Chimera - A visualization system for exploratory research and analysis. J. Comput. Chem. *25*, 1605–1612.

Pruyne, D., Evangelista, M., Yang, C., Bi, E., Zigmond, S., Bretscher, A., and Boone, C. (2002). Role of formins in actin assembly: Nucleation and barbed-end association. Science *297*, 612–615.

Richter, K.N., Revelo, N.H., Seitz, K.J., Helm, M.S., Sarkar, D., Saleeb, R.S., D'Este, E., Eberle, J., Wagner, E., Vogl, C., et al. (2018). Glyoxal as an alternative fixative to formaldehyde in immunostaining and super-resolution microscopy. EMBO J. *37*, 139–159.

Riedl, J., Crevenna, A.H., Kessenbrock, K., Yu, J.H., Neukirchen, D., Bista, M., Bradke, F., Jenne, D., Holak, T.A., Werb, Z., et al. (2008). Lifeact: a versatile marker to visualize F-actin. Nat. Methods *5*, 605–607.

Rizvi, S.A., Neidt, E.M., Cui, J., Feiger, Z., Skau, C.T., Gardel, M.L., Kozmin, S.A., and Kovar, D.R. (2009). Identification and characterization of a small molecule Inhibitor of formin-mediated actin assembly. Chem. Biol. *16*, 1158–1168.

Rosell, F.I., and Boxer, S.G. (2003). Polarized absorption spectra of green fluorescent protein single crystals: Transition dipole moment directions. Biochemistry *42*, 177–183.

Santella, L., Limatola, N., Vasilev, F., and Chun, J.T. (2018). Maturation and fertilization of echinoderm eggs: Role of actin cytoskeleton dynamics. Biochem. Biophys. Res. Commun. *506*, 361–371.

Sosa, H., Peterman, E.J.G., Moerner, W.E., and Goldstein, L.S.B. (2001). ADP-induced rocking of the kinesin motor domain revealed by single-molecule fluorescence polarization microscopy. Nat. Struct. Biol. *8*, 540–544.

Swaminathan, V., Kalappurakkal, J.M., Mehta, S.B., Nordenfelt, P., Moore, T.I., Koga, N., Baker, D.A., Oldenbourg, R., Tani, T., Mayor, S., et al. (2017). Actin retrograde flow actively

aligns and orients ligand-engaged integrins in focal adhesions. Proc. Natl. Acad. Sci. U. S. A. *114*, 10648–10653.

Terada, S., Nakata, T., Peterson, A.C., and Hirokawa, N. (1996). Visualization of slow axonal transport in vivo. Science *273*, 784–788.

Terada, S., Kinjo, M., and Hirokawa, N. (2000). Oligomeric tubulin in large transporting complex is transported via kinesin in squid giant axons. Cell *103*, 141–155.

Tiede, C., Tang, A.A.S., Deacon, S.E., Mandal, U., Nettleship, J.E., Owen, R.L., George, S.E., Harrison, D.J., Owens, R.J., Tomlinson, D.C., et al. (2014). Adhiron: A stable and versatile peptide display scaffold for molecular recognition applications. Protein Eng. Des. Sel. *27*, 145–155.

Vrabioiu, A.M., and Mitchison, T.J. (2006). Structural insights into yeast septin organization from polarized fluorescence microscopy. Nature *443*, 466–469.

Vrabioiu, A.M., and Mitchison, T.J. (2007). Symmetry of septin hourglass and ring structures. J. Mol. Biol. *372*, 37–49.

Wesolowska, N., Avilov, I., Machado, P., Geiss, C., Kondo, H., Mori, M., and Lénárt, P. (2020). Actin assembly ruptures the nuclear envelope by prying the lamina away from nuclear pores and nuclear membranes in starfish oocytes. eLife *9*, e49774.

Winder, S.J., Hemmings, L., Maciver, S.K., Bolton, S.J., Tinsley, J.M., Davies, K.E., Critchley, D.R., and Kendrick-Jones, J. (1995). Utrophin actin binding domain: analysis of actin binding and cellular targeting. J. Cell Sci. *108*, 63–71.

Winn, M.D., Ballard, C.C., Cowtan, K.D., Dodson, E.J., Emsley, P., Evans, P.R., Keegan, R.M., Krissinel, E.B., Leslie, A.G.W., McCoy, A., et al. (2011). Overview of the CCP4 suite and current developments. Acta Crystallogr. Sect. D Biol. Crystallogr. *67*, 235–242.

Zhao, Y., Araki, S., Wu, J., Teramoto, T., Chang, Y.-F., Nakano, M., Abdelfattah, A.S., Fujiwara, M., Ishihara, T., Nagai, T., et al. (2011). An expanded palette of genetically encoded Ca^{2+} indicators. Science *333*, 1888–1891.